International Journal of Nanomedicine

Dovepress
Taylor & Francis Group

Open Access Full Text Article

ORIGINAL RESEARCH

MOF-Mediated Aloe-Emodin Delivery Enhances Hepatocellular Carcinoma Immunotherapy via Pyroptosis and Immunosuppressant Synergy

Huaying Xie*, Xiaoyuan Yi*, Kunzhao Huang, Jianzhang Luo, Qingyu Zeng, Feifei He, Liyan Wang

Digestive Department, Affiliated Hospital of Guilin Medical University, Guilin, 541001, People's Republic of China

*These authors contributed equally to this work

Correspondence: Liyan Wang, Affiliated Hospital of Guilin Medical University, Lequn Road No. 15, Xiufeng District, Guilin, 541001, People's Republic of China, Tel +86 15295953938, Email 168wangliyan@163.com

Purpose: Hepatocellular carcinoma (HCC) remains a major global oncological burden, with conventional therapies showing limited efficacy. This study aimed to utilize pyroptosis to alleviate the tumor's immunosuppressive microenvironment, enhance systemic immunity, and improve immunotherapy efficacy, focusing on precise selection of pyroptosis inducers, immunotherapeutic agents, and drug delivery strategies.

Methods: After synthesizing AE-FeMn/FA, its morphology, particle size, and Zeta potential were characterized. We evaluated its catalytic performance in activating H_2O_2 to produce ·OH, ability to trigger cellular pyroptosis, and in vitro/in vivo anti-tumor effects. Combined with BMS-202, we explored suppression of the PD-1/PD-L1 complex and synergistic induction of pyroptosis.

Results: Intravenous AE-FeMn/FA targeted HCC, with controlled AE release triggering pyroptosis and anti-tumor immunity. BMS-202 alleviated immunosuppression, enhancing AE-FeMn/FA-induced anti-tumor responses, achieving synergistic immune-mediated cancer cell elimination.

Conclusion: The synergistic approach of pyroptosis combined with an enhanced immunotherapy nanoplatform shows promise as an effective HCC immunotherapy strategy, with significant clinical translation potential. Future studies will optimize the platform and conduct clinical trials.

Keywords: aloe-emodin, microenvironment response, pyroptosis, immunosuppressor, BMS-202

Introduction

The development of immune checkpoint blockade therapy (ICB) has witnessed exponential growth in recent years, translating into significant clinical benefits and novel treatment strategies for patients with advanced malignancies.[1,2] This treatment modality exerts dual - pronged anti - tumor effects: it directly targets cancer cells with cytotoxic activity while concurrently activating and recruiting immune cells. By orchestrating this immunostimulatory cascade, it significantly strengthens the host's endogenous anti - tumor immune defenses.[3,4] Despite significant advancements in cancer therapy, numerous critical challenges persist in clinical practice: The response rate to single-agent ICB therapy remains low among most patients with solid tumors. For instance, the response rate to single-agent ICB in hepatocellular carcinoma is less than 20%, which is closely associated with low tumor immunogenicity and the influence of an immunosuppressive microenvironment.[5] Additionally, systemic administration is prone to inducing immune-related adverse events such as colitis and pneumonia, while primary or acquired drug resistance tends to emerge during long-term treatment.[6] Furthermore, macromolecular ICB antibodies exhibit poor tissue penetration and fail to efficiently accumulate in the deep microenvironment of solid tumors, thereby further restricting the full exertion of therapeutic efficacy.[7] Notably, the tumor immune - suppressive microenvironment (TME) poses a significant hurdle, as it often dampens the effectiveness of immunotherapeutic interventions, thereby limiting treatment outcomes.[8,9] The TME harbors

Received: 8 May 2025
Accepted: 28 August 2025
Published: 23 September 2025

a unique set of conditions, including hypoxic stress, acidic extracellular environments, and limited nutrient availability. These factors collectively modify immune cell activity and disrupt critical signal transduction networks in tumor cells, thereby hindering the immune system's capability to recognize and annihilate malignant cells.[10,11] A novel mode of inflammatory cell death, known as cell pyroptosis, has been reported as an immune-assisted strategy mediated by gasdermin-induced cell lysis.[12] This biological mechanism involves the breach of cell membrane integrity, causing the following release of components within the cells. These released substances trigger the activation of cytotoxic lymphocytes, which then actively seek out and eliminate tumor cells.[13,14] The interplay between cell pyroptosis and tumor immunotherapy has become a focal point in oncology research. This mechanism has shown great potential as an effective approach for improving cancer treatment outcomes, providing new insights into immunomodulatory strategies.

Metal ion-mediated immunotherapy, particularly utilizing transition metal ions Fe^{3+} and Mn^{2+}, can interact with hydrogen peroxide present in the tumor microenvironment to generate oxidative species, specifically reactive oxygen species (ROS).[15–17] These ROS not only activate the inflammasome as a secondary signal but also facilitate chemodynamic therapy and induce immunogenic cell death.[18] During pyroptosis, the secretion of immunosuppressive cytokines paradoxically facilitates robust immunogenic cell death. This process initiates the liberation of antigens associated with tumors and specific to tumors, while simultaneously exposing "danger signals" that activate the immune system. This, in turn, activates dendritic cell maturation, induces tumor-specific T cell immune responses, and ultimately eradicates tumor cells.[19,20] However, the rapid clearance of free Fe^{3+} and Mn^{2+} in the body, along with the abundant quantity of glutathione in the neoplastic microenvironment, neutralizes the reactive oxygen species, limiting the efficacy of the immune response.[21,22] To address this challenge, researchers have explored delivery strategies for Fe^{3+} and Mn^{2+}, particularly focusing on the development of nanoplatforms that enable targeted delivery and efficient release in the tumor microenvironment.[23] Metal-organic framework (MOF) nanoparticles have emerged as highly promising candidates for serving as metal sources and drug transportation vehicles in ROS - initiated pyroptosis, mainly because of their remarkably large specific surface area and unique porous structure. This unique structural feature endows them with remarkable capabilities to encapsulate and deliver therapeutic agents efficiently, while also enabling the controlled release of metals essential for triggering pyroptotic pathways.[24,25]

Aloe emodin (AE), an anthraquinone molecule extracted from a diverse range of plant species in nature, has risen to prominence as a key area of scientific investigation. Its wide - ranging pharmacological properties, encompassing counter - inflammatory, antioxidant, and tumor - inhibiting capabilities, have propelled it to the forefront of research in drug discovery and therapeutic development.[26,27] AE exhibits a wide range of anti-tumor properties by inhibiting the synthesis of DNA, RNA, as well as proteins in malignant cells, blocking the growth progression of cancer cells, and restricting cancer cell metastasis, thereby demonstrating its anti-tumor potential.[28–30] Current research has explored nanodelivery systems for AE, such as liposomes and polymeric nanoparticles. These studies have confirmed that nanocarriers can enhance the water solubility of AE, prolong its circulation time, and improve tumor accumulation.[31–33] Nevertheless, the limited aqueous solubility and suboptimal bioavailability of AE currently pose significant obstacles to its translation into clinical practice, hindering the realization of its full therapeutic potential.[34] Consequently, it is crucial to investigate different approaches for increasing its solubility and optimizing its transport to the tumor location. Folate (FA), a naturally occurring ligand that binds to the folate receptor (FR), has been extensively studied as a targeting ligand for nanoparticle delivery owing to its high affinity, small size, and non-toxicity.[35–37]

Guided by the insights discussed earlier, this study employs FA-modified FeMn-MOF as the carrier: The FA ligand can specifically bind to folate receptors highly expressed on tumor cells, enabling active targeted delivery of AE and thereby reducing off-target toxicity; The porous structure of MOFs allows for efficient loading of AE and triggers precise drug release by leveraging characteristics of the tumor microenvironment (such as acidic pH and high H_2O_2 levels); Meanwhile, the FeMn nanoskeleton possesses Fenton-like catalytic activity, which can induce ROS generation and synergistically enhance antitumor efficacy with the inherent pharmacological effects of AE. The synthesis procedure is schematically illustrated in Scheme 1. The nanoparticle synthesis process is simple and efficient, substantially enhancing the solubility of aloe emodin, Fe^{3+}, and Mn^{2+} in water, while also exhibiting excellent biocompatibility. Upon intravenous administration, AE-FeMn/FA nanoparticles can be transported and accumulated at the tumor site, where the nanoparticles rapidly degrade due to the weak acidity and reductive conditions of the tumor microenvironment,

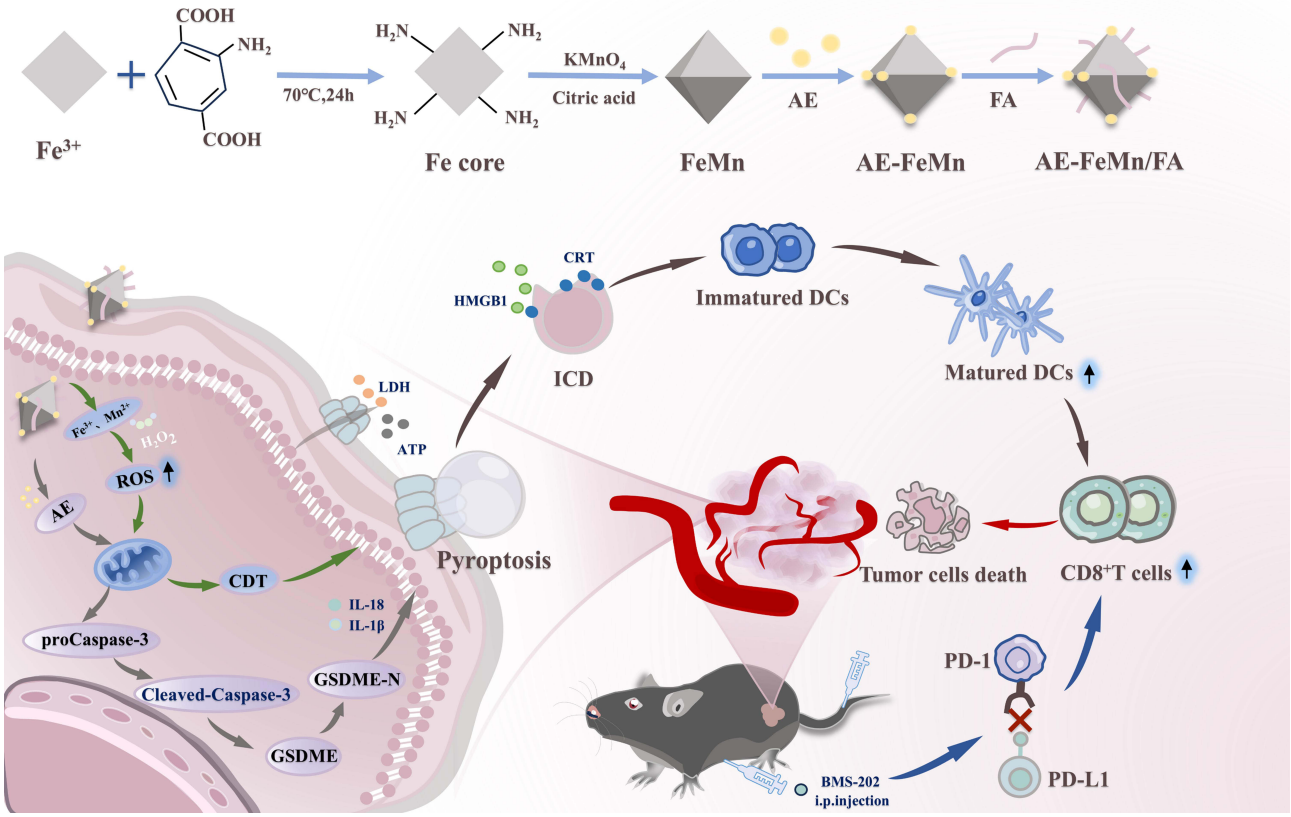

Scheme 1 Schematic representation of the molecular mechanisms by which AE-FeMn/FA exerts antitumor effects through pyroptosis and immunoregulation.

releasing AE, Fe^{3+}, and Mn^{2+}. These metal ions (Fe^{3+} and Mn^{2+}) not only induce inflammasome activation through the formation of ROS, caspase-3 cleavage, and pyroptosis induction in conjunction with AE but also enhance immunogenic cell death triggered by ROS and pyroptosis. This mechanism triggers the recruitment of additional dendritic cells, enabling them to efficiently recognize tumor cells. Subsequently, this process initiates antigen - specific T cellular invasion into the neoplastic microenvironment, ultimately culminating in the establishment of a potent anti - tumor immune reaction. Laboratory - based and animal model studies have demonstrated the significant advantages of our engineered AE-FeMn/FA nanoparticles in inhibiting tumor growth, especially when integrated with the small molecule PD-1/PD-L1 immunosuppressant BMS-202. As a result, the application of AE-FeMn/FA nanoparticles realizes the synergistic immunotherapeutic effect of the bimetallic organic framework and AE-induced pyroptosis, enhancing immunogenic cell death, and providing a new method for the treatment of immunosuppressed tumors.

Materials and Methods

Material

All chemicals, including aloe-emodin, anhydrous ethanol, and methanol, were purchased from the Chemical Company of Chengdu Kelong. For biological assays, the ATP Assay Kit, along with Alexa Fluor 488- and Secondary antibodies tagged with Cyanine 3 (Cy3), were sourced from Beyotime. The DyLight™ 680-conjugated fluorescent secondary antibody was obtained by procurement from Cell Signaling Technology, Inc. (CST). Epizyme Biomedical Technology Co., Ltd. For cell analysis, the FITC - conjugated Annexin V apoptosis assay kit, calcein acetoxymethyl/ propidium iodide viability testing kit, 2′,7′-dichlorodihydrofluorescein diacetate fluorescent probes, JC-1-based mitochondrial membrane potential measurement kit, and extra radioimmunoprecipitation assay lysis buffer were procured from

https://doi.org/10.2147/IJN.S533216

Beyotime located in Shanghai, China. Finally, NeoBioscience Biotechnology Co., LTD. provided ELISA kits for mouse TNF-α, IL-1β, IL-18, and IFN-γ, enabling the quantification of key cytokines in the study.

Antibodies and Kits

True-Nuclear™ Mouse Treg Flow™ Kit (FOXP3 APC), catalog number [320029, BioLegend], was used at a dilution ratio of 1:200. Brilliant Violet 510™-conjugated anti-mouse CD4 antibody (clone GK1.5), catalog number [320029, BioLegend], was used at a dilution ratio of 1:200. PE-labeled anti-mouse/human CD11c antibody, catalog number [FC0480, Signalway Antibody], was used at a dilution ratio of 1:300.HMGB1 rabbit monoclonal antibody (catalog number ab79823, ABclonal) was used at a dilution ratio of 1:1000 for Western blot analysis and 1:500 for immunofluorescence (IF) experiments.CRT rabbit monoclonal antibody (catalog number A20986, ABclonal) was used at a dilution ratio of 1:500 for IF experiments. β-actin rabbit monoclonal antibody (catalog number 66009-1-Ig, Proteintech Group) was used at a dilution ratio of 1:5000 for Western blot analysis.NLRP3 rabbit polyclonal antibody (catalog number obtained from ABclonal official website) was used at a dilution ratio of 1:1000–1:2000 for Western blot analysis and 1:100–1:300 for immunohistochemistry (IHC) experiments. It was utilized to detect the expression and changes of NLRP3 protein, which is of great significance for studying inflammation-related signaling pathways.Caspase-3 rabbit monoclonal antibody (catalog number obtained from ABclonal official website) was used at a dilution ratio of 1:1000–1:3000 for Western blot analysis and 1:50–1:200 for immunocytochemistry (ICC)/IF experiments. It was employed to detect the activation and expression of Caspase-3 protein, which is closely related to the process of cell apoptosis.GSDME rabbit monoclonal antibody (Cat. #40618S, Cell Signaling Technology) was used at a dilution ratio of 1:1000 for Western blot analysis.N-GSDME rabbit monoclonal antibody (Cat. #40618S, Cell Signaling Technology) was used at a dilution ratio of 1:1000 for Western blot analysis.CD86 monoclonal antibody (catalog number 65592-1-MR, Proteintech) was used at a dilution ratio of 1:200.CD80 monoclonal antibody (catalog number 98384-1-RR, Proteintech) was used at a dilution ratio of 1:300.

Methods

Synthesis of AE-FeMn/FA

Briefly, $FeCl_3 \cdot 6H_2O$ (2.5 mmol) and H_2BDC (3.75 mmol) were dissolved in N, N-dimethylformamide (DMF, 15 mL) and stirred at room temperature for 10 minutes using a magnetic stirrer. Subsequently, the mixture was stirred at 70°C for 24 hours. After the reaction, the mixture was centrifuged at 12,000 rpm for 10 minutes, and the resulting precipitate was collected. The precipitate was sequentially washed with DMF (50 mL × 3), ethanol (50 mL × 3), and ultrapure water (50 mL × 3), with centrifugation performed after each washing step to collect the precipitate. The collected precipitate was redispersed uniformly in ultrapure water (40 mL) via ultrasonication. An appropriate amount of $KMnO_4$ solution (10 mg/mL) was added dropwise to the above dispersion, and the reaction was allowed to proceed for 2 hours. Subsequently, a suitable volume of citric acid solution (1.5 mg/mL) was added dropwise, and the mixture was stirred at room temperature for 24 hours using a magnetic stirrer. The precipitate was then collected by centrifugation at 12,000 rpm for 10 minutes. The collected precipitate was redispersed uniformly in ultrapure water. AE (1 mg) was dissolved in 1 mL of dimethyl sulfoxide (DMSO), and the AE solution was added to the precipitate dispersion. The mixture was stirred at room temperature for 24 hours, followed by centrifugation at 13,000 rpm for 15 minutes to collect the precipitate. The resulting precipitate was redispersed uniformly in ultrapure water via ultrasonication. Folic acid (FA, 5 mg) was dissolved in 1 mL of 0.1 M NaOH and diluted with 4 mL of ultrapure water. The pH was adjusted to 7.4 using 0.1 M HCl. Under sonication, the FA solution was added dropwise to the AE-FeMn dispersion. Subsequently, 1-ethyl-3-(3-dimethylaminopropyl) carbodiimide (EDC, 10 mg) and N-hydroxysuccinimide (NHS, 6 mg) were added to activate carboxyl groups on FA for covalent conjugation to surface amino groups on FeMn-MOF. The reaction proceeded at room temperature for 24 h under gentle stirring. The final product, AE-FeMn/FA, was collected by centrifugation (12,000 rpm, 10 min), washed thoroughly with ultrapure water to remove unreacted reagents, and stored at 4°C.

Determination of Drug Encapsulation Efficiency and Loading Capacity of AE

The encapsulation efficiency (EE) and drug loading capacity (LC) of AE were determined using high-performance liquid chromatography (HPLC), with the specific procedures as follows:

After the synthesis of AE-FeMn/FA, unloaded free AE was separated from the nanoparticles by ultracentrifugation (13,000 rpm, 15 minutes). The supernatant containing free AE was collected, and the precipitate was resuspended in ultrapure water for subsequent analysis. Appropriate HPLC conditions were set. A series of AE standard solutions with known concentrations were prepared, and their peak areas were measured to establish a linear regression equation correlating peak area with AE concentration.

Calculations:

Encapsulation Efficiency (EE, %)= $\frac{TotalAE-FreeAE}{TotalAE}\times 100\%$

Drug Capacity (LC, %)= $\frac{TotalAE-FreeAE}{Mass\ of\ nanoparticles}\times 100\%$

All measurements were performed in triplicate, and the results are expressed as mean ± standard deviation.

AE Release Kinetics Assay

Exactly 5 mg of AE-FeMn/FA nanoparticles were accurately weighed and dispersed in 5 mL of release medium, which included phosphate-buffered saline (PBS, pH 7.4) and acetate buffer (pH 5.5, simulating the intracellular lysosomal environment). The dispersion was transferred into a dialysis bag (molecular weight cutoff: 3.5 kDa), which was then sealed and immersed in a centrifuge tube containing 45 mL of the corresponding release medium. The centrifuge tube was placed in a constant-temperature shaker at 37°C with continuous oscillation at 100 rpm. Samples (5 mL each) were collected at 0, 1, 2, 4, 8, 12, and 24 hours, and an equal volume of fresh release medium was replenished immediately after each sampling to maintain a constant total volume. The concentration of AE in the released medium was determined using HPLC, and the cumulative release rate was calculated accordingly. Each pH group was performed in triplicate, and the results are expressed as mean ± standard deviation.

Characterizations

The size and shape of FeMn and AE-FeMn/FA nanoparticles were examined by transmission electron microscopy (TEM), meanwhile, the DLS - based size distribution and the Zeta potential were quantified with a Malvern Zetasizer. The absorbance of FeMn, AE, AE-FeMn, and AE-FeMn/FA in the wavelength range of 250–600 nm was identified by means of ultraviolet - visible spectrometers (Metash, UV - 5500PC). Additionally, the UV-visible absorption spectra of AE and AE-FeMn/FA were also obtained.

Cell Lines and Animals

The Hepa1 - 6 and Hepa1 - 6 - Luci hepatocellular carcinoma cell lines were acquired from Wuhan Pricella Biotechnology Co., Ltd. Hepa1 - 6 - Luci and Hepa1 - 6 cells were grown in Dulbecco's Modified Eagle Medium (DMEM) supplemented with 10% fetal bovine serum (FBS) and 1% penicillin - streptomycin mixture. These cell cultures were maintained under a humidified environment at 37°C with 5% CO_2 to ensure optimal growth conditions. Four - week - old C57BL/6 mice were acquired from the Experimental Animal Center of Guilin Medical University. All procedures involving animals were executed according to the standards and provisions approved by the Ethics Committee of Hospital of Guilin Medical University (Approval No. GLMC202303112). In subsequent cell experiments, unless otherwise specified, the concentrations of the drugs used are as follows: AE at 10 μM; FeMn, AE-FeMn, and AE-FeMn/FA at 25 μg/mL. For animal experiments, the dosages are as follows: AE at 30 mg/kg; FeMn, AE-FeMn, and AE-FeMn/FA at 80 mg/kg; and BMS-202 at 5 mg/kg.

Cell Viability Assays

The Hepa1 - 6 and THLE - 2 cell cultures were placed in 96 - well plates at a density of 7000 cells per well and left to grow overnight. According to the experimental design, different concentrations of FeMn, AE-FeMn, and AE-FeMn/FA were introduced into the cells, followed by 24 hours for incubation. The drug-free control group was included as a baseline for comparison. The CCK8 assay was employed to determine cell viability. The results were statistically analyzed by utilizing GraphPad Prism 9 software.

Cellular Uptake

To assess the uptake of AE-FeMn/FA nanoparticles by Hepa1-6 cells, we seeded the cells in multi-well plates and allowed them to attach. FCM - based cell analysis and inverted fluorescence microscopy were utilized to systematically analyze the cellular uptake of AE-FeMn/FA. Specifically, 1 mg of AE-FeMn/FA was combined with 1 mg of Rhodamine B (RhB), followed by vigorous stirring and centrifugation to generate RhB-encapsulated AE-FeMn/FA nanoparticles. Hepa1-6 cells were subsequently incubated together with RhB-loaded AE-FeMn/FA nanoparticles at specified time points (0 h, 1 h, 2 h, 4 h, and 8 h) to determine the temporal pattern of nanoparticle uptake. Post-incubation, the cells received a sequence of washings with fresh PBS to eliminate extracellular nanoparticles. Intracellular localization of AE-FeMn/FA was evaluated by means of an inverted fluorescence microscope. For better visualization of cellular structures, The cell nuclei underwent staining with Hoechst 33342 at a concentration of 10 μg/mL for 10 minutes before microscopic observation. Additionally, cells incubated with RhB-loaded AE-FeMn/FA at the same time points as in the previous experiment were subjected to fluorescence intensity measurement using FCM. For the experimental arrangement, the excitation wavelength was adjusted to 488 nm and the emission wavelength to 525 nm in order to accurately record the fluorescence signals. This measurement allowed for a quantitative assessment of the internalized AE-FeMn/FA.

Alive/Dead Cell Staining Experiment

Hepa1 - 6 cell lines were plated in 6 - well plates at a seeding density of 100,000 cells per well and incubated overnight. Subsequently, the cells were separated into various treatment groups.: I) Control; II) FeMn; III) AE; IV) AE-FeMn; V) AE-FeMn/FA. After incubating the cells for 24 hours, they underwent staining with calcein - AM and propidium iodide (PI) over 15 minutes. Ultimately, the stained cell samples were subjected to detailed observation and quantitative analysis with the employment of an inverted fluorescence microscope. This method enabled the accurate discrimination between viable and non - viable cells based on their distinct fluorescence characteristics.

EdU - Based Cell Proliferation Assay

Hepa1 - 6 cells were plated in 48 - well plates at a seeding density of 1.5×10^5 cells per well. After allowing the cells to attach, they were treated differently and cultured for a duration of 24 hours. To assess cell proliferation, the cells were labeled according to the EdU kit guidelines. Subsequently, the cells were immobilized with a 4% paraformaldehyde solution to preserve cell morphology. The proliferating cells were labeled with the EdU reagent, while the nuclei were stained with the DAPI reagent. Fluorescent pictures of the dyed cells were captured via an inverted fluorescence microscope. Subsequently, ImageJ software was employed to perform a measurement - based analysis of Cells positive for EdU, enabling the determination of relative cell multiplication levels across various treatment conditions.

TUNEL Staining Analysis

The Hepa1-6 cell specimens were seeded in 24-well plates and remained for 24 hours to adhere. After this initial incubation, the cells were given treatments as per the experimental protocol. Next, the cells were flushed with PBS and then preserved using 4% paraformaldehyde for 25 minutes. To facilitate antibody penetration, the cells' permeability was induced using a 0.3% Triton X-100 PBS solution. Subsequently to permeabilization, 100 μL of a thoroughly mixed TUNEL detection reagent was introduced into each well, and the plates were cultivated at 37 degrees Celsius in the dark for 60 minutes. To eliminate residual, unbound reagents, the cells experienced three successive cleansings with PBS. Next, inverted fluorescence microscopy was employed to visualize and identify apoptosis - exhibiting cells, which were characterized by the occurrence of fragmented DNA.

Assay for Cell Apoptosis

Hepa1-6 cells (1×10^6 cells per well) were inoculated into 6 - well plates and grown for 24 hours. Following the incubation period, the cells were subjected to different treatments, resulting in the following groups: I) Control; II) FeMn; III) AE; IV) AE-FeMn; V) AE-FeMn/FA. Subsequently, the culturing medium was carefully aspirated, and the cells underwent a gentle washing with PBS. After trypsinization, the cells were collected by centrifugation and then suspended again in generate a homogeneous suspension of individual cells. For the assessment of apoptosis, the cells were treated

with 5 μL of Annexin V - FITC solution and kept in the dark for 15 minutes. Following this, 10 μL of PI solution was introduced, and the cells were stained at 4°C for 10 minutes. Apoptotic cells were then quantitatively analyzed by means of a flow cytometer.

Intracellular ROS Detection

To evaluate the cellular oxidative stress status, FCM and fluorescence microscopy were employed as analytical tools. Specifically, the Hepa1 - 6 cells were categorized into five experimental groups: I) Control; II) FeMn; III) AE; IV) AE-FeMn; V) AE-FeMn/FA. Following the treatment, the cells were incubated with the 2′,7′ - dichlorofluorescein diacetate (DCFH - DA) probe for half an hour to measure the production of ROS. Following the incubation with the DCFH - DA probe, FCM was employed to measure the fluorescence intensity. The wavelengths for excitation and emission were accurately adjusted to 488 nm and 525 nm respectively, respectively, to accurately detect the signals generated by the probe. For a more detailed microscopic analysis, the cell samples were subjected to further processing. First, they were incubated with DAPI for 10 minutes to selectively stain the cell nuclei. This step allowed for clear visualization of the nuclear structure within the cells. After staining, the samples were gently rinsed two times with PBS to remove any unbound DAPI, ensuring that the background fluorescence was minimized. Finally, the prepared specimens were examined using a fluorescence microscope. Through analyzing the fluorescence configurations and magnitudes, we were able to assess the extent of oxidative stress within the cells. This dual - approach using FCM and microscopic examination provided a comprehensive understanding of the cellular oxidative stress response to the different treatments.

GSH Assay

The glutathione content within Hepa1-6 cells was measured using Sulfur Trace™ Violet. Hepa1 - 6 cells were inoculated in 24 - well plates and kept for a 24 - hour incubation period. Following the experimental design, the cells underwent various treatments: I) Control; II) FeMn; III) AE; IV) AE-FeMn; V) AE-FeMn/FA. Subsequently, the cells were dyed using Thiotracker™ violet staining solution at a concentration of 20 μM in the dark for 30 minutes and subsequently rinsed with PBS to eliminate any non - attached dye. In order to assess the GSH level, the intracellular fluorescence was detected using a reversed fluorescence microscope.

Mitochondria Integrity Assay in vitro

To assess mitochondrial integrity, initially, Hepa1-6 cells were seeded within 24 - well culture dishes and incubated for one night. Subsequently, those cells were divided into five treatment groups: I) Control; II) FeMn; III) AE; IV) AE-FeMn; V) AE-FeMn/FA. Following the treatment, the existing growth medium was carefully eliminated, and those cells were gently cleansed using PBS prior to the addition of fresh medium. Finally, each well received 1 mL of JC - 1 staining solution to evaluate mitochondrial transmembrane potential. Subsequently, the stained cells were transferred to a cell incubator maintained at 37°C for continued incubation. Once the incubation was complete, those cells were rinsed three times with the JC-1 staining buffer to remove any unbound dye molecules. Finally, an inverted fluorescence microscope was employed to visualize and analyze the morphological and functional alterations in mitochondria.

Western Blot Assay

Hepa1 - 6 cells were plated in 6 - well plates and grown until fully adherent before being subjected to various treatments. The experimental setup included five groups: I) Control; II) FeMn; III) AE; IV) AE-FeMn; V) AE-FeMn/FA. Upon completion of the treatment, the culture medium was discarded, and those cells were washed thoroughly with PBS. To extract cellular proteins, Proteases were added to the RIPA lysis buffer. An equivalent quantity of protein (ranging from 20 to 50 μg) from each group were fractionated by polyacrylamide gel electrophoresis at 200 V for 30 minutes. Subsequently, the resolved proteins were transferred to polyvinylidene difluoride (PVDF) membranes with a constant current of 400 mA for a duration ranging from 20 to 60 minutes. Once blocking was completed, the membranes were left to incubate at 4°C throughout the night with particular primary antibodies. After washing, the membranes were probed with Label the fluorescent secondary antibody in the dark. β - actin was selected as the internal reference. Finally, the expression of the target protein was visualized for detection. ImageJ software (version 2.0.0) was employed to conduct

semi - quantitative analysis of the protein bands, enabling the comparison of protein expression levels among different experimental groups.

Immunofluorescence Staining

Hepa1 - 6 cell lines were inoculated within 24 - well culture plates and incubated for one day to permit cell attachment and early growth. Following the established experimental design, the cells were treated with the designated agents. After the treatment cycle, the culture substrate was carefully aspirated, and gently rinse the cells with PBS. Next, fix the cells with 4% paraformaldehyde for 30 minutes. Subsequently, incubate the cells with the primary antibody overnight. Following this, the cells were incubated with Cy3-coupled secondary antibodies (Beyotime, cat. no. A0516 and A0423) at room temperature for 1 hour. To visualize the cell nucleus, DAPI dye was applied for 10 minutes. Finally, capture fluorescent images using a confocal microscope, and measure the relative fluorescence intensity of each image with ImageJ software.

Assay of ATP

Hepa1 - 6 cells were inoculated into 6 - well plates and then subjected to diverse treatment conditions: I) Control, II) FeMn, III) AE, IV) AE-FeMn, and V) AE-FeMn/FA. After 24 hours, the cell supernatant was collected and centrifuged. The amount of extracellular ATP was measured according to the instructions provided by the ATP detection kit.

Detection of LDH

LDH (lactate dehydrogenase) activity was determined with a commercial LDH detection kit as per the manufacturer's guidelines. Briefly, the assay involved the transformation of lactate into pyruvate catalyzed by LDH, with the concomitant conversion of NAD^+ into NADH. The speed of NADH generation was determined by spectrophotometry at a wavelength of 340 nm. The LDH activity was computed according to the alteration in absorbance over time and expressed as units per liter (U/L) of enzyme activity.

In - Body Fluorescence Imaging of Tumor Tissues

Five - week - old C57BL/6 mice bearing tumors were randomly split into two groups. They were given an injection of Cy5.5-FeMn or Cy5.5-FeMn/FA (dose: 5 mg/kg) through the tail vein. Fluorescent images were captured at different times using an infrared imaging system. Upon the humane termination of the mice, vital organs such as the cardiac tissue, hepatic parenchyma, splenic pulp, pulmonary lobes, renal cortex, and neoplastic growths were carefully excised. These specimens were then prepared for ex vivo fluorescence imaging to assess nanoparticle accumulation and distribution.

Bioluminescence Imaging

Tumor volume dynamics in C57BL/6 mice were monitored using bioluminescence imaging (PerkinElmer, USA). Specifically, 20 μL of the Luc1 substrate (DTZ solution) was administered via intraperitoneal injection to tumor - bearing mice. Three minutes after injection, the mice were put under anesthesia with tribromoethanol. Subsequently, the anesthetized animals were carefully placed in the imaging chamber, and bioluminescence images were captured and stored for further analysis.

In - vivo Therapeutic Experiment

C57BL/6 mice were subcutaneously inoculated with Hepa1-6-Luci cells. Therapeutic interventions were initiated when tumor volume reached approximately 100 mm^3, ensuring a standardized baseline for evaluating treatment efficacy. First set of tumor treatment efficacy experiments: A total of 5 groups (n=6 per group): I) Control, II) FeMn, III) AE, IV) AE-FeMn, and V) AE-FeMn/FA. Different formulations were administered via tail vein injection on days 0, 3, 6, 9, 12, and 15. Throughout the treatment period, tumor size and weight were monitored regularly. In addition to caliper measurements, bioluminescence imaging (PerkinElmer, USA) was used to assess dynamic changes in tumor volume. On day 19 of the experiment, mice were humanely euthanized in accordance with approved ethical guidelines. Tumor tissues and major organs (heart, liver, spleen, lungs, and kidneys) were carefully harvested for subsequent histological, biochemical, and pathological analyses. Tumor tissues were evaluated using immunofluorescence staining (TUNEL, NLRP3, Cleaved-Caspase-3, HMGB1) and flow cytometry (CD11c, CD80, CD86, CD3, CD8). Harvested heart, liver, spleen, lungs, and

kidneys were processed for histopathological examination with hematoxylin-eosin (H&E) staining, a standard method for visualizing tissue morphology and cellular architecture. Meanwhile, serum samples were collected from experimental animals and prepared for enzyme-linked immunosorbent assay (ELISA) to quantify specific blood biomarkers.

Second set of combination therapy and survival analysis experiments: A total of 4 groups: G1) Control, G2) BMS-202, G3) AE-FeMn/FA, and G4) AE-FeMn/FA+ BMS-202. On days 0, 3, 6, 9, 12, and 15, PBS or AE-FeMn/FA was administered via the caudal vein. BMS-202 was injected into the G2 and G4 groups from days 1 to 9. On day 19, the mice were terminated, then tumor tissue and blood specimens were gathered. For the survival analysis subgroup, each group included 10 mice (n=10). Furthermore, the survival of administered with the various drugs mentioned above G1) Control, G2) BMS-202, G3) AE-FeMn/FA, and G4) AE-FeMn/FA+ BMS-202) was analyzed. From each group, ten mice with tumors were chosen and observed for 45 days. The experimental endpoint was reached when the size of the tumor hit 1500 mm^3 or in the event of the mice's demise.

Flow Cytometric Analysis

Surgical excision was performed on the inguinal and axillary lymph nodes of tumor - carrying mice, and then they were instantly soaked in 1 mL of PBS. Using the end of a 1 - mL syringe, the lymph nodes were gently pulverized until the solution became turbid, facilitating the release of cells. The cell suspension that resulted from the process was then passed across a 40 - micrometer cell strainer to eliminate tissue remnants, followed by centrifugation at 1000 g for 3 minutes. Subsequently, filtered out tissue fragments and blocked with 5% bovine serum albumin (BSA) for 20 minutes to minimize unspecific binding. Those cells were then incubated with flow cytometry antibodies against CD11c, CD80, and CD86 for 20 minutes. Ultimately, flow cytometry was carried out to evaluate the activation state of DCs in the lymph nodes of mice.

Tumor tissues harvested from mice were immersed in 2 mL of RPMI 1640 medium. Using sterile scissors, the tissue samples were finely minced and subsequently transferred to a digestion solution composed of collagenase IV (1 mg/mL), hyaluronidase (0.2 mg/mL), and DNAse I (0.2 mg/mL). Subsequently, this blend was placed in a water bath maintained at 37°C and left for 60 minutes. Following digestion, the cell suspension formed was filtered via a 40 - micrometer cell strainer to eliminate unliquefied tissue residues, subsequently, the fluid obtained from filtration was centrifuged at 800 times the force of gravity for 5 minutes to sediment the cells. The cell suspension was slowly introduced to the individual cell dispersion at a volume ratio of 2:1, into a centrifuge tube pre-filled with the individual working solution, and centrifuged at 20°C for 30 min. The underlying cells were removed, washed once with PBS, closed with 5% BSA solution for 20 minutes, subsequently, it was dyed using anti - CD3 and anti - CD8 antibodies for flow cytometry for half an hour. The invasion of immune cells into the tumor was detected by flow cytometry.

Cytokine Detection

After administering the different treatments, orbital venous blood specimens were obtained from the mice. The blood specimens were allowed to coagulate for 60 minutes. Then, spun at 3000rpm for 15 minutes to isolate the blood serum for experimental analysis. The levels of cytokines in mouse serum samples were quantified using commercially available ELISA kits. All procedures were meticulously performed in strict compliance with the detailed instructions provided by the kit manufacturers to ensure accurate and reliable results.

Hemolytic Test

To evaluate the hemolytic potential of AE - FeMn/FA, blood specimens were obtained from the orbital cavity of mice. The mice were treated with AE - FeMn/FA with differing concentrations (0, 50, 100, 150, 200, 250, 300 μg/mL). After collection, the blood samples were spun at 3500 rpm for 10 minutes to obtain the upper liquid layer. The optical density of each supernatant was determined at 540 nm by employing a spectrophotometer. The rate of hemolysis was computed in accordance with the formula: Hemolysis rate (%) = (A - A0)/(A∞ - A0) ×100%, in which A denotes the absorbance of the AE - FeMn/FA - treated group, A0 represents the absorbance of the control group using PBS, meanwhile, A∞ represents the absorbency of the deionized - water - based control group.

Safety Evaluation of Biology

To evaluate the biological safety of the nanomaterials in C57BL/6 mice (n=3), blood specimens were obtained from tumor-bearing mice for biochemical analysis of hepatic and renal function, including ALT, AST, CREA, UREA, CK-MB, LDH1, among others. Following collection, the most important organs were immediately placed in a 4% formaldehyde method for appropriate fixation, which maintained the structural integrity of the tissues. After the fixation process, the organs were stained with hematoxylin and eosin.

Data Analytics

GraphPad Prism software (Version 9) was utilized to conduct all statistical analyses. For multi - group comparisons, one - way ANOVA or two - way ANOVA was employed, whereas the student's *t* - test was used to conduct pairwise comparisons between two groups. The experimental data are reported as the average plus or minus the standard deviation. Significant statistical difference was signified as follows: *P < 0.05, **P < 0.01, ***P < 0.001, and ****P < 0.0001.

Results

Synthesis and Characterization of AE-FeMn/FA

A metal-organic framework (FeMn-MOF) was synthesized by reducing potassium permanganate (KMnO4) doped manganese with citric acid (CA), resulting in the successful preparation of FeMn-MOF.[17] Subsequently, AE was loaded into the FeMn-MOF framework via physical adsorption, and FA was coated on its surface through amide bond conjugation, ultimately forming AE-FeMn/FA nanoparticles. TEM analysis revealed that AE-FeMn exhibited a typical rhomboidal crystalline structure with clear edges, good dispersibility, and no obvious aggregation. After FA modification, AE-FeMn /FA retained the rhomboidal core structure, with a uniform particle size distribution (average particle size: 147 nm) and stable dispersion state (Figure 1A and B). Further elemental distribution analysis demonstrated that Fe and Mn elements in AE-FeMn/FA were uniformly distributed in the core region of the rhomboidal particles, while N elements (a characteristic element derived from FA) were mainly enriched on the particle surface. This elemental evidence confirms the successful synthesis of the FeMn metal framework and the effective modification of FA (Figure 1C). AE's UV absorption spectra displayed prominent characteristic peaks at 450 nm (Figure S1), while FeMn-MOF alone did not show any AE characteristic peaks, confirming the successful encapsulation of AE (Figure 1D). The high-performance liquid mass spectrometer measured a loading ratio of AE at 40.55%. Particle size and potential analysis indicated that the particle size of AE-FeMn/FA was approximately 147.7 nm, with a negative charge, suggesting its relative stability in blood circulation (Figure 1E and F). Drug release behavior of AE-FeMn/FA was studied using dialysis in tumor and physiological environments. In pH 7.4 PBS representing the physiological environment, AE release was minimal, reaching only 12.7% within 24 hours, indicating its stability in blood. Conversely, in the acidic pH 5.5 environment simulating the tumor, AE release was rapid, with a cumulative release of 74.28% within 24 hours, suggesting the rapid degradation of AE-FeMn/FA under acidic conditions and laying the foundation for controlled drug release (Figure 1G). FeMn-MOF could generate acutely noxious ROS, through the Fenton reaction.[38,39] In vitro experiments using tetramethylbenzidine (TMB) demonstrated effective ROS production by FeMn-MOF, which increased with higher AE-FeMn/FA concentration (Figure 1H and I). AE-FeMn/FA also exhibited increased ROS generation under acidic conditions, high TMB concentration, and excess H_2O_2 (Figure 1J–L, respectively). In tumor cells, ROS production is often accompanied by the consumption of glutathione (GSH) to regulate REDOX balance. Due to the presence of Fe and Mn, intracellular GSH was further depleted. GSH consumption was assessed through the DTNB experiment, which showed that the amount of GSH consumed by AE-FeMn/FA gradually increased over time (Figure 1M). Comparing the GSH consumption capacity of various nanoparticle groups, it was observed that at the same concentration, AE-FeMn/FA exhibited significantly higher GSH degradation than FeMn alone, indicating its effective consumption of GSH (Figure S2).

Tumor Cell Uptake and Cytotoxicity of AE-FeMn/FA

Based on the successful synthesis of AE-FeMn/FA, the nanoparticle exhibits small size, stability in the blood, and the capacity to catalyze the creation of ROS and consume GSH. Next, the cytotoxicity in a laboratory setting the prepared material was assessed using Hepa1-6 mouse hepatoma cells. To elucidate the interplay of the nanoscale particles with cancer

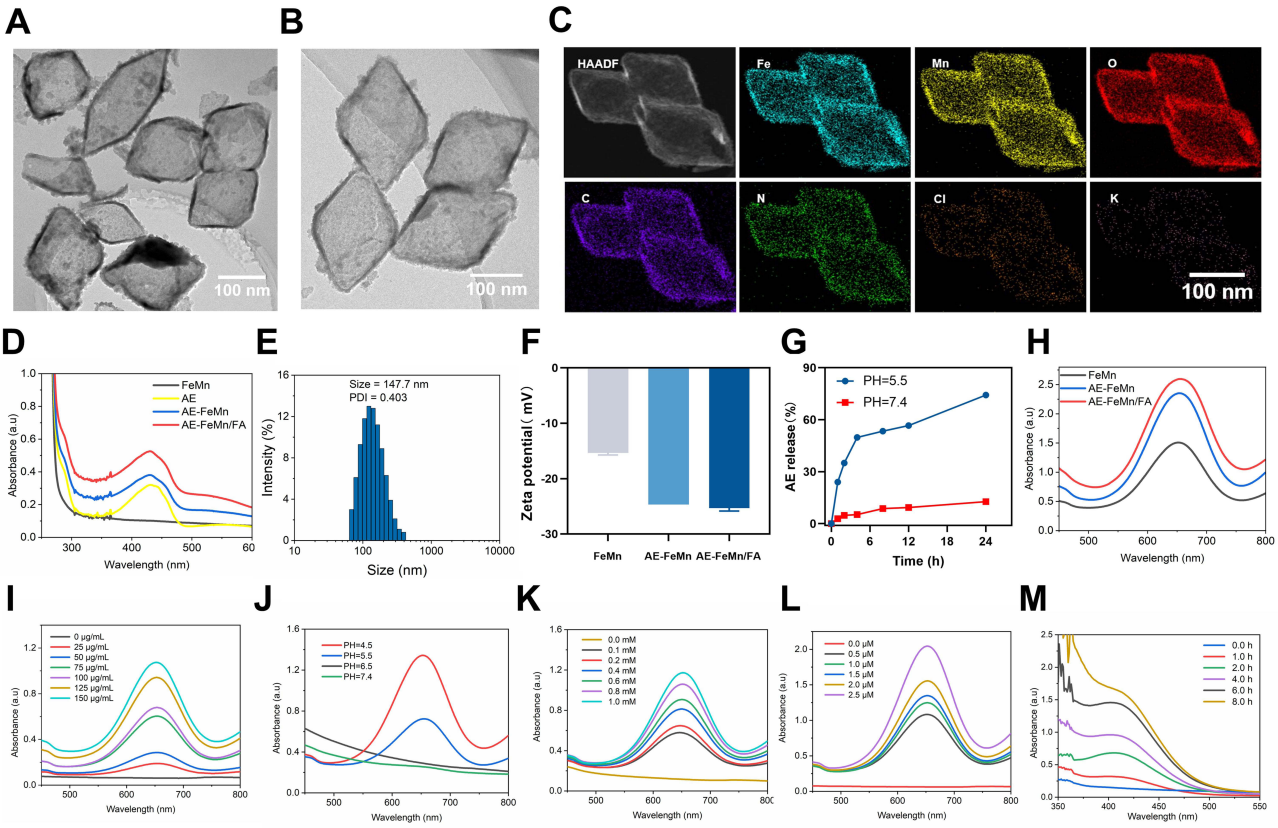

Figure 1 Synthesis and Characterization of AE-FeMn/FA Nanoparticles. (**A**) TEM image of FeMn. (**B**) TEM image of AE-FeMn/FA. (**C**) Elemental mapping of AE-FeMn/FA. (**D**) UV-Vis absorption spectra of FeMn, AE, AE-FeMn, and AE-FeMn/FA. (**E**) Hydrodynamic diameter of AE-FeMn/FA. (**F**) Zeta potential measurements for FeMn, AE-FeMn, and AE-FeMn/FA. (**G**) Release profiles of AE under various conditions. (**H**) UV-Vis absorption spectra of FeMn, AE-FeMn, and AE-FeMn/FA, including (**I**) spectra under different AE-FeMn/FA concentrations, (**J**) spectra at varying pH levels, (**K**) spectra in the presence of different concentrations of MTB, (**L**) spectra with varying concentrations of H_2O_2, and (**M**) GSH consumption over time.Scale bar=100 nm.

cells, Rhodamine-labeled AE-FeMn/FA was co-cultured with Hepa1-6 cells. Fluorescence inverted microscopy analysis showed that the strength of intracellular red fluorescence steadily rose as time elapsed. Specifically, the fluorescence attained its maximum after 8 hours of incubation, suggesting that the nanomaterials efficiently accumulated within the tumor cells (Figure 2A). This result indicated successful uptake of the nanoparticles by Hepa1-6 cells, laying the foundation for further cytotoxicity studies. The quantitative data obtained from cytometric flow assay analysis validated the results of fluorescence microscopy observations, as shown in Figure 2B. Prompted by the remarkable cellular uptake ability, we evaluated the cytotoxicity of different drugs targeted at tumors against Hepa1 - 6 cells. Live cell/dead cell staining demonstrated the significant killing effect of AE-FeMn/FA on Hepa1-6 cells (Figures 2C and S3). Following 24 hours of cultivation, the survival ability of cells after AE - FeMn and AE - FeMn/FA treatment was considerably lower compared to that of the FeMn group, evidencing that the targeted synergistic effect of AE and FA enhanced the killing effect of tumor cells (Figure 2D). Co-incubation with normal hepatocytes THLE-2 revealed that AE-FeMn/FA had no effect on THLE-2 cell viability, indicating tumor-specific cytotoxicity (Figure S4). Additionally, cell proliferation assays (Figure 2E and F) and Tunel staining (Figure 2G and H) further confirmed the significant killing and proliferation inhibition effects of AE-FeMn/FA on tumor cells. Flow cytometry results also supported this conclusion (Figure 2I and J). Collectively, these data demonstrate that AE-FeMn/FA can selectively target Hepa1-6 cells and induce ROS in the intracellular acidic environment.

https://doi.org/10.2147/IJN.S533216

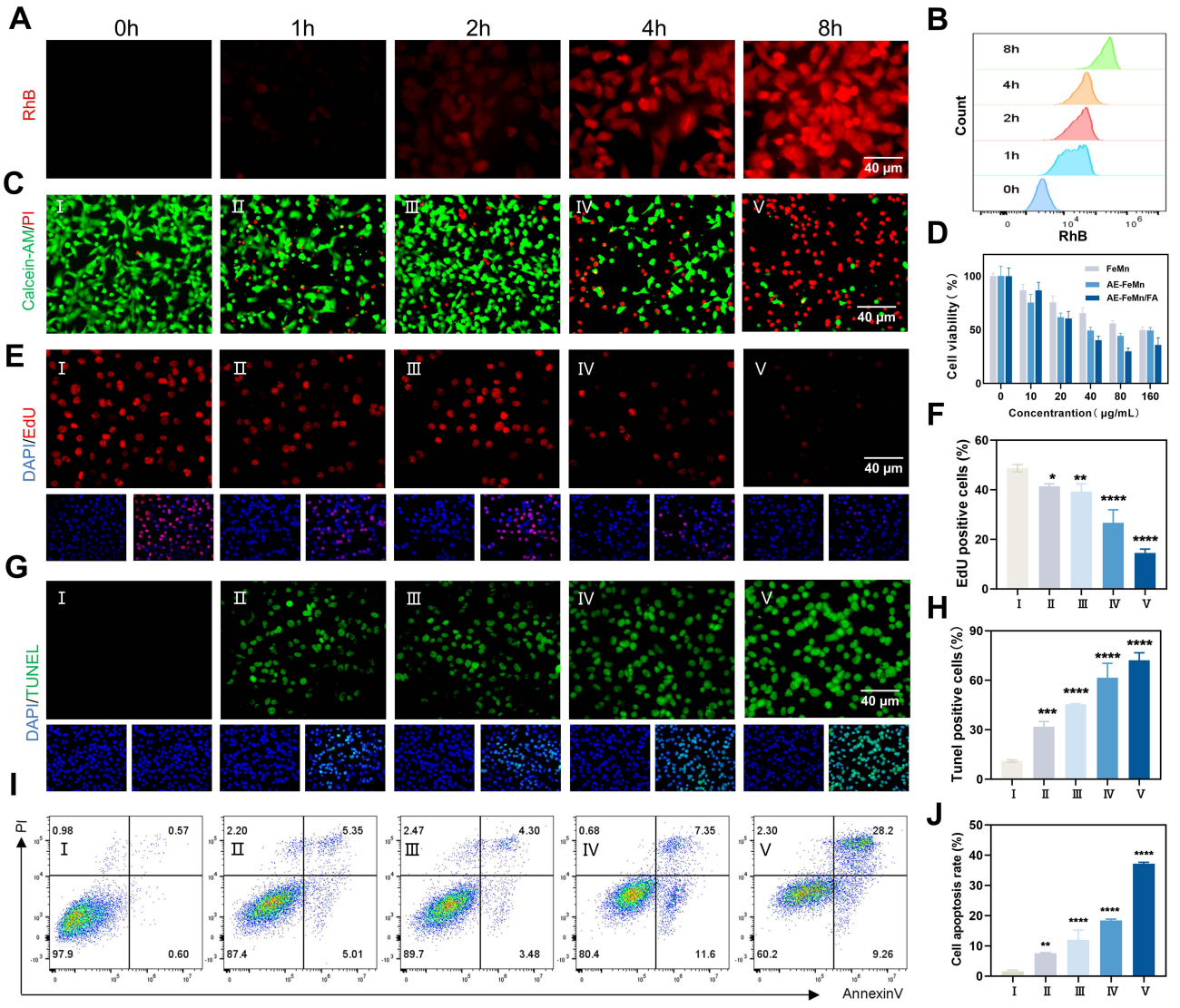

Figure 2 Cellular Uptake and Cytotoxicity of AE-FeMn/FA Nanoparticles. (**A**) Inverted fluorescence microscopy images and (**B**) flow cytometry analysis demonstrating the time-dependent uptake of AE-FeMn/FA by Hepa1-6 cells. (**C**) Inverted fluorescence microscopy images of live/dead cell staining, showing viability (Calcein-AM, green signal) and cell death (PI, red signal) in Hepa1-6 cells following treatment. (**D**) Cytotoxicity assessment of Hepa1-6 cells after 24-hour incubation with various drug formulations. Cell proliferation images (**E**) and (**F**) fluorescence quantification results indicating the proliferation of Hepa1-6 cells treated with different formulations.(**G**) TUNEL staining images and (**H**) fluorescence quantification results demonstrating apoptosis in Hepa1-6 cells treated with various formulations.(**I**) Flow cytometry analysis illustrating apoptosis in Hepa1-6 cells post-treatment and (**J**) fluorescence quantification results.Scale bar: 40 μm. (n=3, *P < 0.05, **P < 0.01, ***P < 0.001, ****P < 0.0001). (I: Control; II: FeMn; III: AE; IV: AE-FeMn; V: AE-FeMn/FA).

AE-FeMn/FA Induced Pyrodeath of Hepa1-6 Cells, Which Resulted in Immunogenic Cell Death

Motivated by the anti-tumor effects of AE-FeMn/FA observed in vitro, we conducted investigations into the intracellular mechanisms in Hepa1-6 cells. It has been demonstrated that in the acidic milieu of tumors, transition metal ions including Fe^{2+} and Mn^{2+} interact with H_2O_2, resulting in the production of significant quantities of ROS (eg, ·OH) through Fenton or Fenton-like reactions. These reactions play a crucial role in tumor tissue and can influence cytotoxicity mediated by chemodynamic therapy (CDT).[40,41] Transition metal ions effectively induce tumor cell death.[42] To explore the ROS production capacity of AE-FeMn/FA in tumor cells, we employed a DCFH-DA probe. The results demonstrated that AE-FeMn/FA significantly catalyzed ROS production in tumor cells compared to the other groups (Figure 3A and B), indicating its ability to promote ROS production. Similarly, flow cytometry results showed stronger ROS fluorescence signals in tumor cells treated with AE-FeMn/FA (Figures S5 and S6). Due to the presence of Mn^{2+} and Fe^{3+}, the

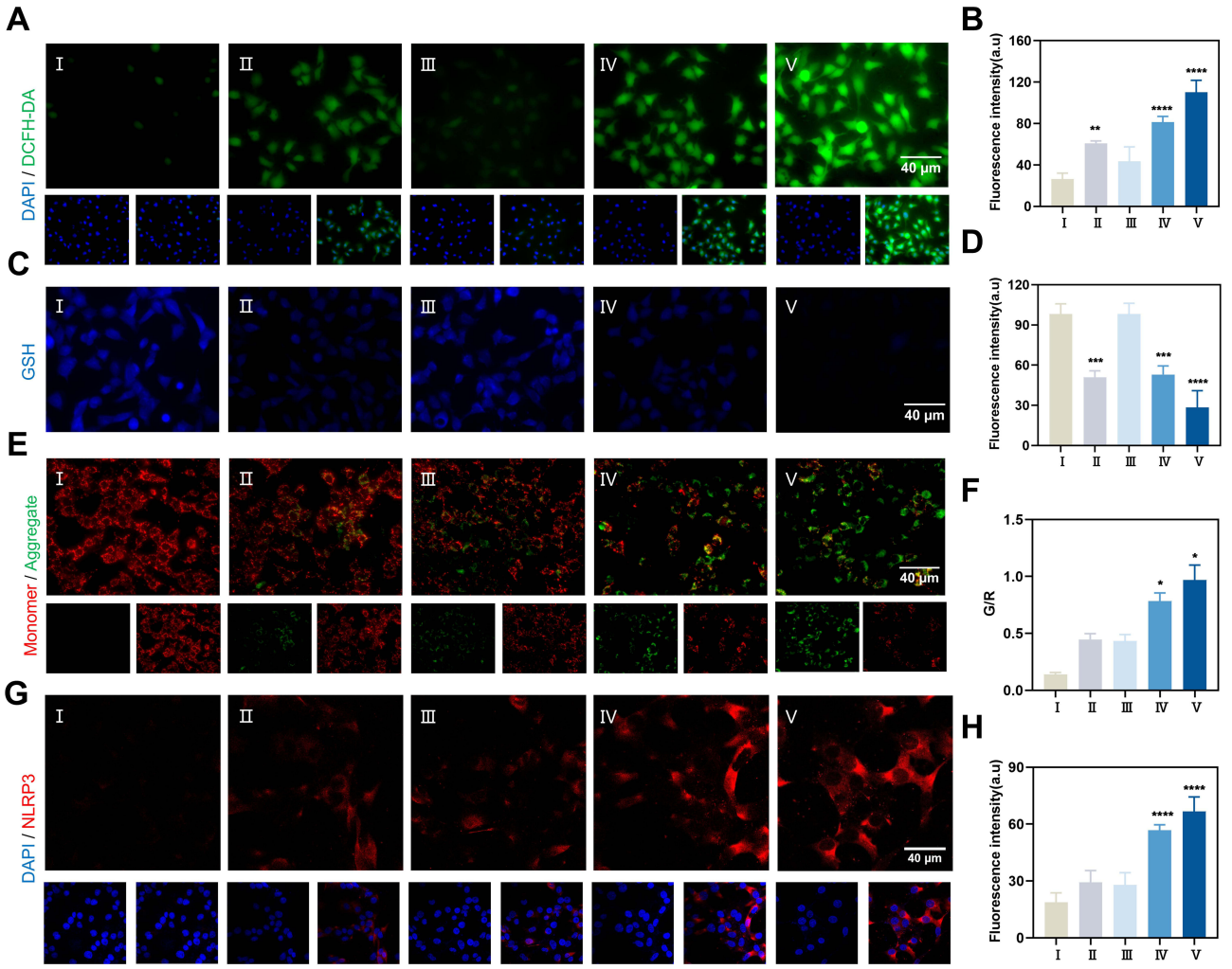

Figure 3 AE-FeMn/FA Induces Pyrodeath in Hepa1-6 Cells Through Redox Regulation. (**A**) Fluorescence microscopy images demonstrating ROS generation, along with (**B**) corresponding semi-quantitative analysis. (**C**) Fluorescent images showing GSH depletion and (**D**) the respective semi-quantitative analysis.(**E**) Fluorescence imaging indicating changes in mitochondrial transmembrane potential under different treatments, with (**F**) quantitative analysis of transmembrane potential variations among treatment groups.(**G**) Immunofluorescence staining of the NLRP3 inflammasome following various treatments, accompanied by (**H**) the corresponding semi-quantitative analysis.Scale bar: 40 μm. (n=3, *P < 0.05, **P < 0.01, ***P < 0.001, ****P < 0.0001). (I: Control; II: FeMn; III: AE; IV: AE-FeMn; V: AE-FeMn/FA).

generation of ·OH is accompanied by the consumption of GSH, maintaining a dynamic redox equilibrium.[39] The experimental results showed consistent GSH consumption and ·OH production in the solutions treated with different nanoparticles (Figure 3C and D). In summary, AE-FeMn/FA can regulate the redox status in tumor cells and modulate Hepa1-6 cells by promoting ROS production and inhibiting GSH levels. Next, we employed JC-1 fluorescent dyes to examine the mechanism of cellular demise and monitor alterations in MMP. JC-1 accumulates and fluoresces red in normal mitochondria, while it appears as a monomer in damaged mitochondria, resulting in a change of red fluorescence to green (Figure 3E). The fluorescence intensity ratio (G/R) of the control group and the AE-FeMn/FA group was approximately 0.14 and 0.96, respectively (Figure 3F), reflecting the mitochondrial state of the cells and unveiling an important mechanism in the process of cellular demise. Pyroptosis is defined by cellular expansion, cell membrane lysis, and the expulsion of intracellular components.[43,44] Furthermore, AE can trigger pyroptosis through gasdermin E (GSDME), and its activation is mediated by caspase-3 cleavage to form pores.[45] Upon treatment of Hepa1-6 cells with AE-FeMn/FA, NLRP3 was significantly upregulated, indicating the activation of pyroptosis (Figure 3G and H). As shown in Figure 4A, after AE-FeMn/FA treatment, the plasma membrane of Hepa1 - 6 cells exhibited significant swelling, leading to cytoplasmic membrane rupture and the liberation of intracellular substances (Figure 4B and C). Subsequently, we analyzed the mechanism related to pyroptosis in Hepa1-6 cells through Western blotting, and the

https://doi.org/10.2147/IJN.S533216

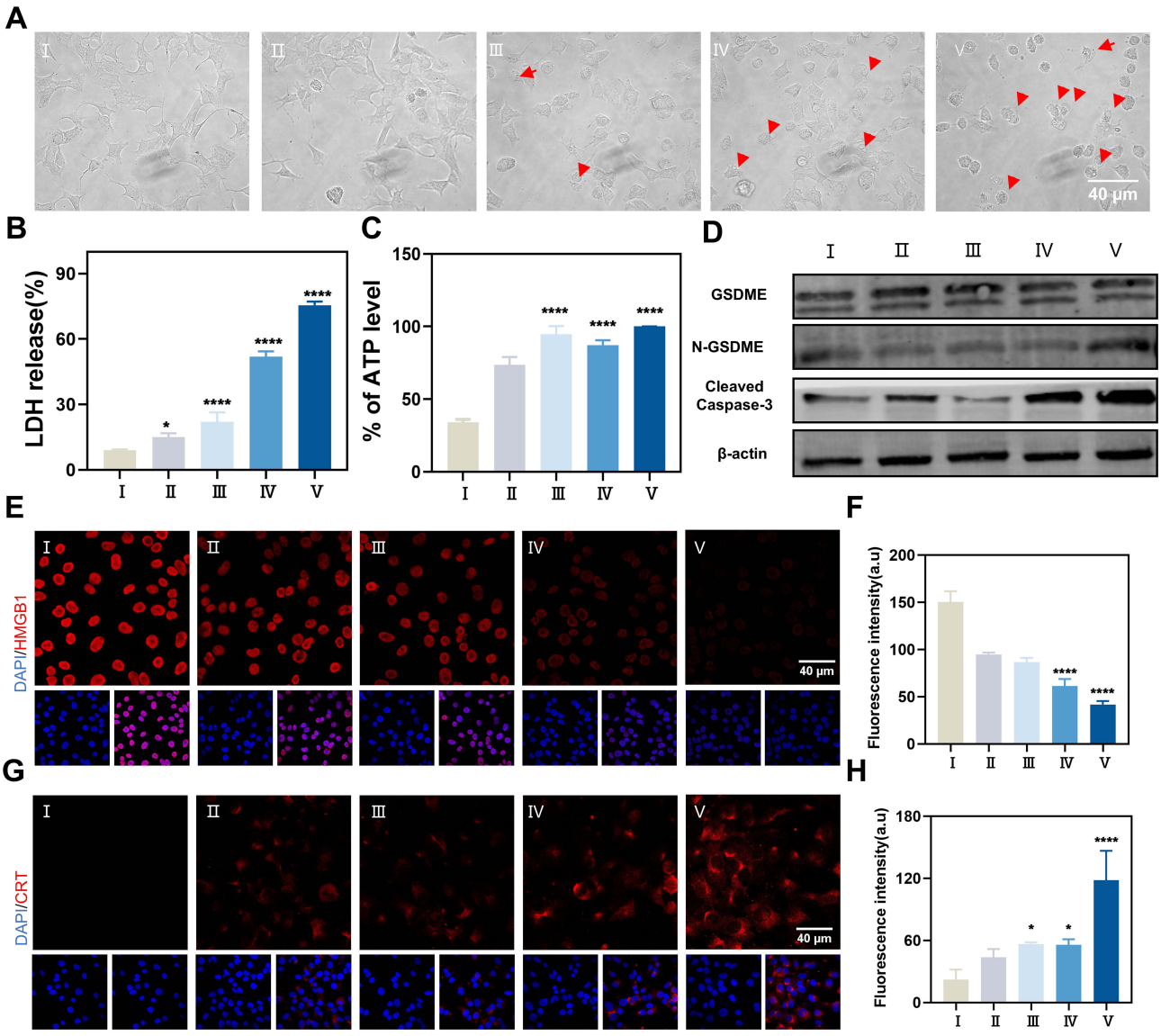

Figure 4 AE-FeMn/FA Induces Pyroptosis and Immunogenic Cell Death in Hepa1-6 Cells Through Redox Regulation. (**A**) Microscopic observations of morphological changes in Hepa1-6 cells following different treatments, with red arrows indicating large bubbles characteristic of pyroptosis cells. (**B**) LDH release from tumor cells after various treatments. (**C**) ATP release from Hepa1-6 cells detected in the supernatant. (**D**)Western blot analysis of pyroptosis related proteins in Hepa1-6 cells subjected to different treatments. (**E**) Representative immunofluorescence images of HMGB1 in Hepa1-6 tumor cells post-treatment, accompanied by quantitative analysis (**F**). (**G**) Representative immunofluorescence images of CRT in Hepa1-6 tumor cells after various treatments, with corresponding quantitative analysis (**H**). Scale bar: 40 μm. (n = 3, *P < 0.05, ****P < 0.0001). (I: Control; II: FeMn; III: AE; IV: AE-FeMn; V: AE-FeMn/FA).

results demonstrated that AE-FeMn/FA-induced pyroptosis was more pronounced (Figure 4D). Pyroptosis belongs to the inflammatory category mode of cellular demise that releases various inflammatory factors and activates an anti-tumor immune response.[12,46] To validate the in vitro immune activation effect of AE-FeMn/FA, we evaluated the ICD effect, as well as the expression of HMGB1 and CRT as biomarkers. The results showed that AE-FeMn/FA significantly enhanced the ICD effect (Figure 4E-H). Additionally, the manifestation of HMGB1 in Hepa1-6 cells was consistent with the immunofluorescence results obtained through Western blot analysis (Figure S7).

In vivo Anti-Tumor Effects of AE-FeMn/FA

The accumulation of pyrogenic inducers in tumors is crucial for enhancing the anti-tumor effect and triggering an immune response.[47] To assess the effectiveness of in vivo tumor therapy, we labeled AE-FeMn and AE-FeMn/FA with the fluorescent probe Cy5.5 and monitored their biodistribution in Hepa1-6 tumor-bearing mice using IVIS spectroscopy

(Figures 5A, B, and S8). The results demonstrated that AE-FeMn/FA accumulated more rapidly and to a greater extent at the tumor site compared to AE-FeMn, and it persisted for 48 hours after injection (Figure S9). Additionally, major organs were collected 48 hours after injection for bioluminescence imaging analysis (Figure S10). The tumor site exhibited higher fluorescence intensity for AE-FeMn/FA compared to AE-FeMn, indicating the good tumor-targeting and sustained retention effect of AE-FeMn/FA, which established the foundation for subsequent treatment experiments. In Hepa1-6 tumor-bearing mice, we further evaluated the anti-tumor efficacy of the metal nanoparticles to explore their potential as an immunotherapy strategy for solid tumors. After inoculation with Hepa1-6 tumors, different therapeutic agents (PBS, FeMn, AE, AE-FeMn, AE-FeMn/FA) were intravenously injected every three days (Figure 5B), moreover, the size of

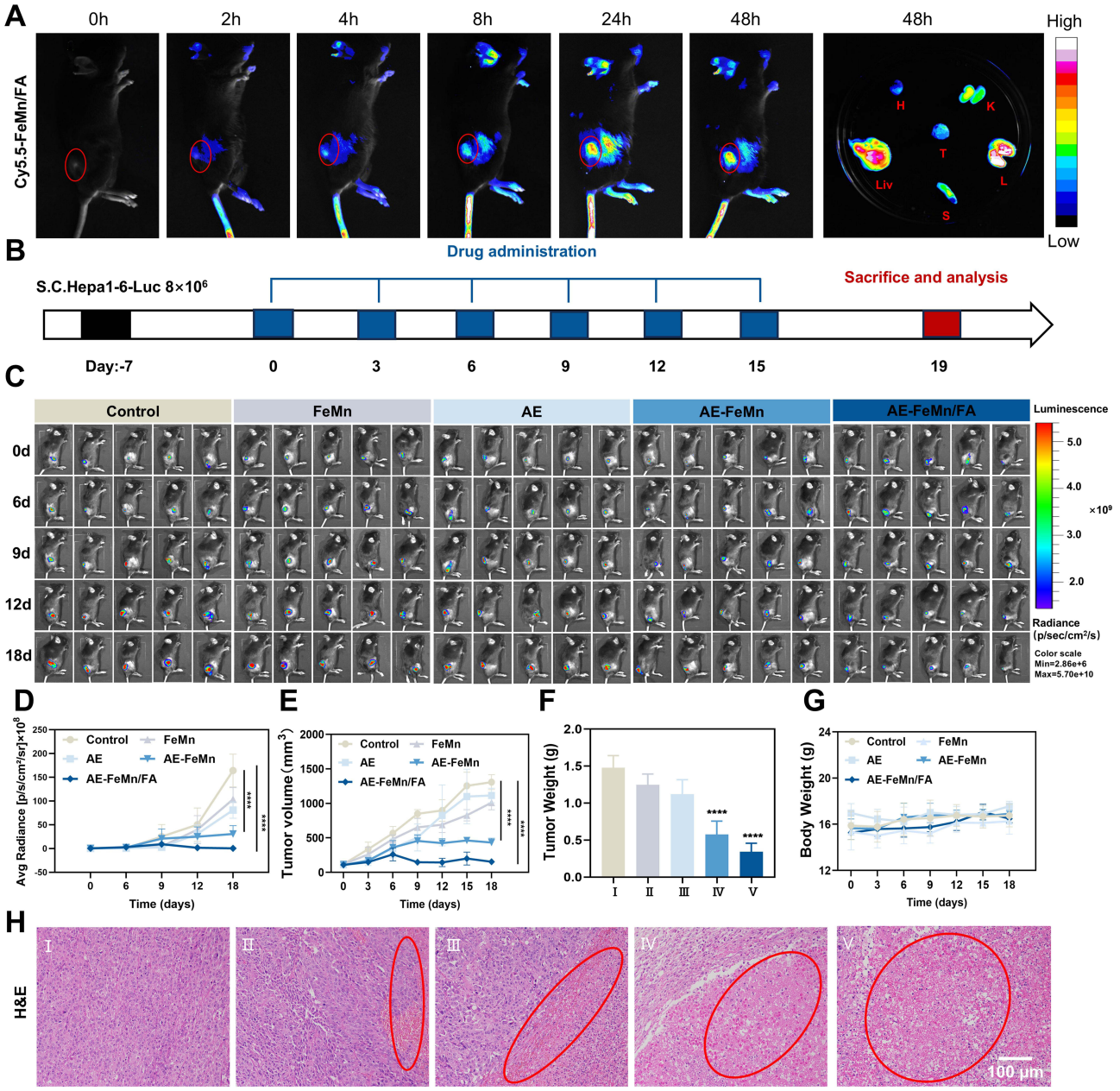

Figure 5 Antitumor effects of AE-FeMn/FA in vivo. (**A**) In vivo and in vitro biodistribution of Cy5.5-labeled AE-FeMn/FA after intravenous injection in Hepa1-6 tumor-bearing mice, with tumor tissue outlined in red. (H: Heart, (K) Kidney, (T) Tumor, (L) Lung, (S) Spleen, Liv: Liver) (**B**) Treatment strategy for AE-FeMn/FA. (**C**) Bioluminescent imaging to monitor tumor growth on days 0, 6, 9, 12, and 18. (**D**) Quantification of bioluminescence. (**E**) Tumor volume variations in each group of Hepa1-6 tumor-bearing mice. (**F**) Tumor weights measured on day 19. (**G**) Changes in body weight of Hepa1-6 tumor-bearing mice across groups. (**H**) Histological evaluation of tumor sections from mice treated with different protocols, stained with H&E, necrotic areas are marked in red. Scale bar: 100 μm. (n=6, ****P < 0.0001). (I:Control; II:FeMn; III:AE; IV:AE-FeMn; V:AE-FeMn/FA).

https://doi.org/10.2147/IJN.S533216

tumors and the weight of mice were measured on a daily basis. The results showed that tumor volume continued to increase in the group treated with PBS, whereas tumor progression occurred significantly inhibited in the AE-FeMn/FA group (Figure 5C–E). Tumor weighing results after treatment demonstrated that the weight of tumors in the AE - FeMn/FA group was markedly less than that in the PBS group and the group with single - metal nanoparticles (Figure 5F), further confirming the enhanced antineoplastic effectiveness of combination therapy. To assess the biosafety of the nanoparticles, we monitored the weight of the murine bodies, which showed minimal alteration throughout the therapy (Figure 5G). Furthermore, in vitro hemolysis experiments demonstrated that AE-FeMn/FA did not cause hemolysis (Figure S11). HE staining was utilized to evaluate the influence of nanoparticles on major organs of mice, and the results showed no significant lesions (Figure S12). Moreover, biochemical indexes of the AE-FeMn/FA group did not show significant differences compared to the control group (Figure S13). These findings indicate that AE-FeMn/FA exhibits good biosafety. To elucidate the antineoplastic mechanism of AE-FeMn/FA, we executed histological staining with hematoxylin and eosin and TUNEL - based immunofluorescence staining on tumor specimens. The findings indicated that the area of tissue damage in the AE-FeMn/FA group was the largest, consistent with the changes in tumor volume (Figure 5H). TUNEL staining further confirmed the severe destruction of tumor tissue (Figures 6A and S14).

Study on Pyrodeath Mechanism of AE-FeMn/FA in Vivo

To further elucidate the mechanism by which AE-FeMn/FA exerts tumor suppression through pyroptotic cell death in animal models, we performed immunofluorescence analysis of NLRP3 and cleaved Caspase-3 (C-Caspase-3) proteins on post-treatment tumor sections. Results showed that the red fluorescent signals of NLRP3 and C-Caspase-3 were significantly upregulated in tumor tissues of the AE-FeMn/FA group (Figures 6B, C and S15, S16). Concurrently, based on the significant ICD effect observed in vitro, we examined the expression of HMGB1 in tumor tissues of Hepa1-6 tumor-bearing mice. Immunofluorescence results revealed a higher degree of extracellular HMGB1 release in the AE-FeMn/FA treatment group (Figures 6D and S17), indicating that the nanoparticles also exert ICD efficacy in vivo. Furthermore, ELISA detection of pyroptosis-related inflammatory factors demonstrated that serum levels of IL-18 and IL-1β in the AE-FeMn/FA treatment group were significantly elevated (Figure 6E and F). These findings further support the conclusion that the metal nanoparticles exert tumor-suppressive effects through pyroptosis, which is consistent with the anti-tumor data observed in vitro. When the ICD effect occurs in tumor cells, it triggers the maturation process of dendritic cells and facilitates their ability to present antigens to T cells, thereby activating the effector T cell response.[48–50] In the present study, ELISA assays demonstrated that the AE-FeMn/FA group induced the release of the cytokine TNF-α, a result that could further activate the proliferation of cytotoxic T cells (Figure 6G). Subsequent flow cytometry analyses confirmed that the number of mature dendritic cells (DCs) was significantly increased in the AE-FeMn/FA group (Figure 6H and I), with a concurrent substantial elevation in the proportion of $CD8^+$ T cells (Figures S18 and S19).

AE-FeMn/FA Combined with Immunosuppressant BMS-202 Enhanced Anti-Tumor Immunity

PD - 1 is present during T lymphocyte activation and expansion, and it reduces the functionality of effector T - lymphocytes by regulating intracellular signaling, thus producing negative modulation of the tumor immune reaction and leading to immune escape of tumor cells.[51,52] Studies have indicated that the small molecule inhibitor BMS-202 can hinder the PD - 1/PD - L1 engagement and boost T cell activation.[53,54] To investigate the effect of the combined application of AE-FeMn/FA and BMS-202 on anti-tumor immunity, we developed a tumor-bearing murine model of Hepa1-6-Luc and arbitrarily partitioned it into four subgroups (n=6): control, BMS-202, AE-FeMn/FA, and AE-FeMn/FA+BMS202. The model establishment and treatment plan are depicted in Figure 7A. In every group, the tumor dimensions and the body weights of the animals were assessed at three - day intervals. The findings indicated that the mixture of AE-FeMn/FA and BMS-202 remarkably inhibited tumor growth, as confirmed by the bioluminescent imaging system tumor volume assessment at different time points (Figure 7B). This outcome was further supported by tumor volume changes (Figure 7C). Moreover, the survival rate of the control group was 0% on day 45, while the survival rate of the combination therapy group remained at 80% by the end of the observation period (Figure 7D), and had little effect on the mass of the mice (Figure S20). The mass of

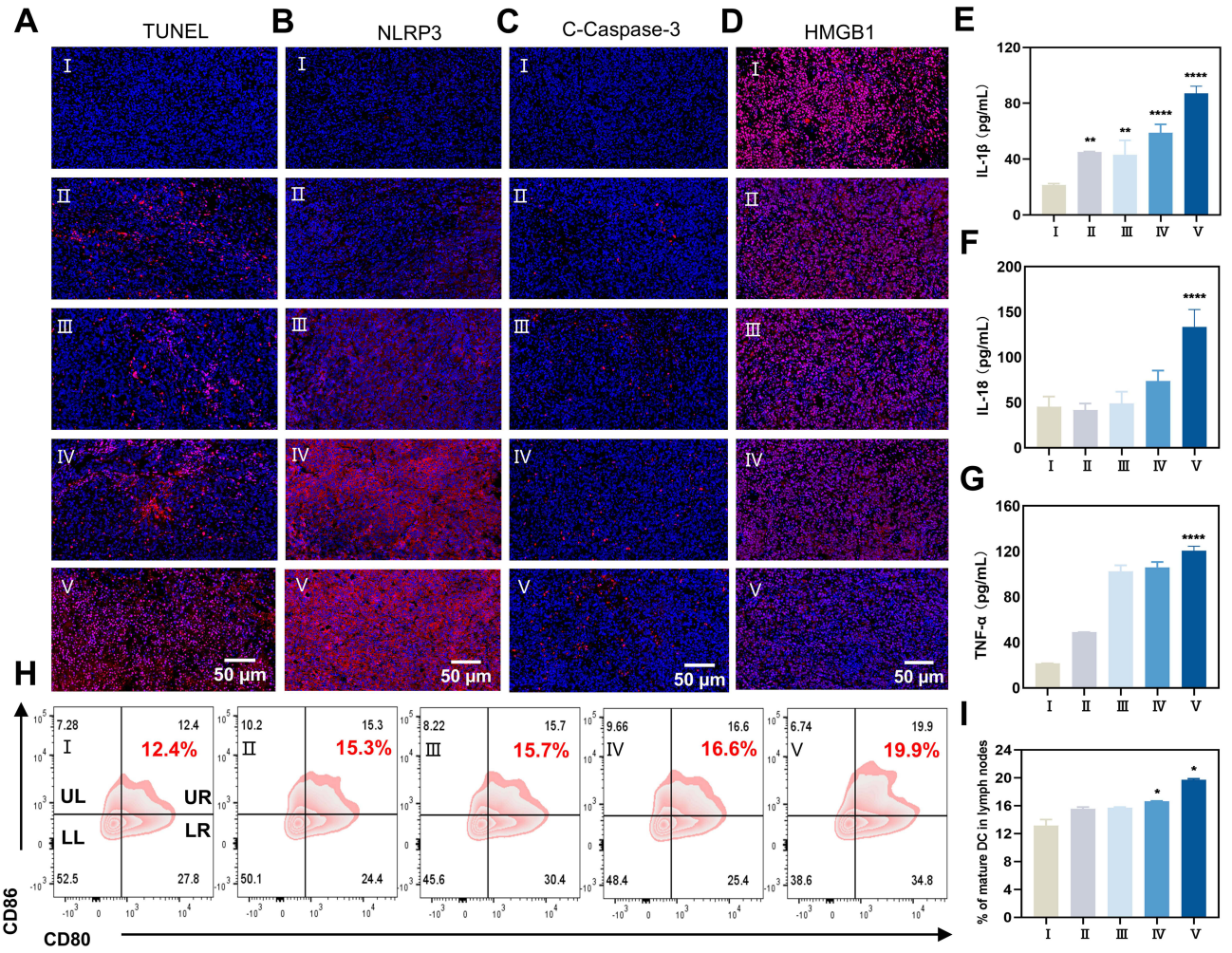

Figure 6 In vivo antitumor effects of AE-FeMn/FA. Immunofluorescent staining of tumor sections from treated groups showing (**A**) TUNEL (red), (**B**) NLRP3 (red), (**C**) C-Caspase-3 (red), and (**D**) HMGB1 (red). Levels of pyroptosis-related cytokines (**E** and **F**) and immune-related cytokines (**G**) in the serum of Hepa1-6 tumor-bearing mice following antitumor treatment. Representative flow cytometry results of mature dendritic cells (CD11c+, CD80+, CD86+) in tumor tissues after different treatments (**H**), along with corresponding quantitative analysis (**I**). Among them: UL ($CD80^-CD86^+$), UR ($CD80^+CD86^+$), LR ($CD80^+CD86^-$), LL($CD80^-CD86^-$). Scale bar: 100 μm. (n=3, *P < 0.05, **P < 0.01, ****P < 0.0001). (I: Control; II: FeMn; III:AE; IV:AE-FeMn; V:AE-FeMn/FA).

the excised tumors also supported these results (Figure 7E), suggesting that the combined immunoagent further enhanced the anti-tumor effect of AE-FeMn/FA. BMS-202 alleviates immunosuppression mainly by inhibiting the assembly of the PD - 1/PD - L1 aggregate. To further validate the immunotherapy efficacy of AE-FeMn/FA+BMS202, we examined serum relevant cytokines following various therapies. The outcomes demonstrated that TNF-α and IFN-β levels were significantly higher in the AE-FeMn/FA+BMS202 group than in the other groups, stimulating cytotoxic T cell infiltration and inducing a systemic immune response (Figure 7F and G). Next, we used flow cytometry to assess the impact of AE-FeMn/FA combined with BMS-202 on the proportion of $CD8^+$T cells. The findings indicated that the proportion of $CD8^+$ T cells reached 43% in the AE-FeMn/FA+BMS202 group, which was significantly higher than the 35.5% in the AE-FeMn/FA group, indicating that the combination treatment significantly increased the level of $CD8^+$ T cell infiltration (Figures 7H and S21).

Discussion

In conclusion, we successfully developed an acid-responsive metal-organic delivery nanoparticle, AE-FeMn/FA, which effectively activates the NLRP3-mediated pyroptosis pathway. Through the release of tumor-specific metal ions, this nanoparticle induces the generation of cytotoxic ROS, inducing cell - programmed death in neoplastic cells.

https://doi.org/10.2147/IJN.S533216

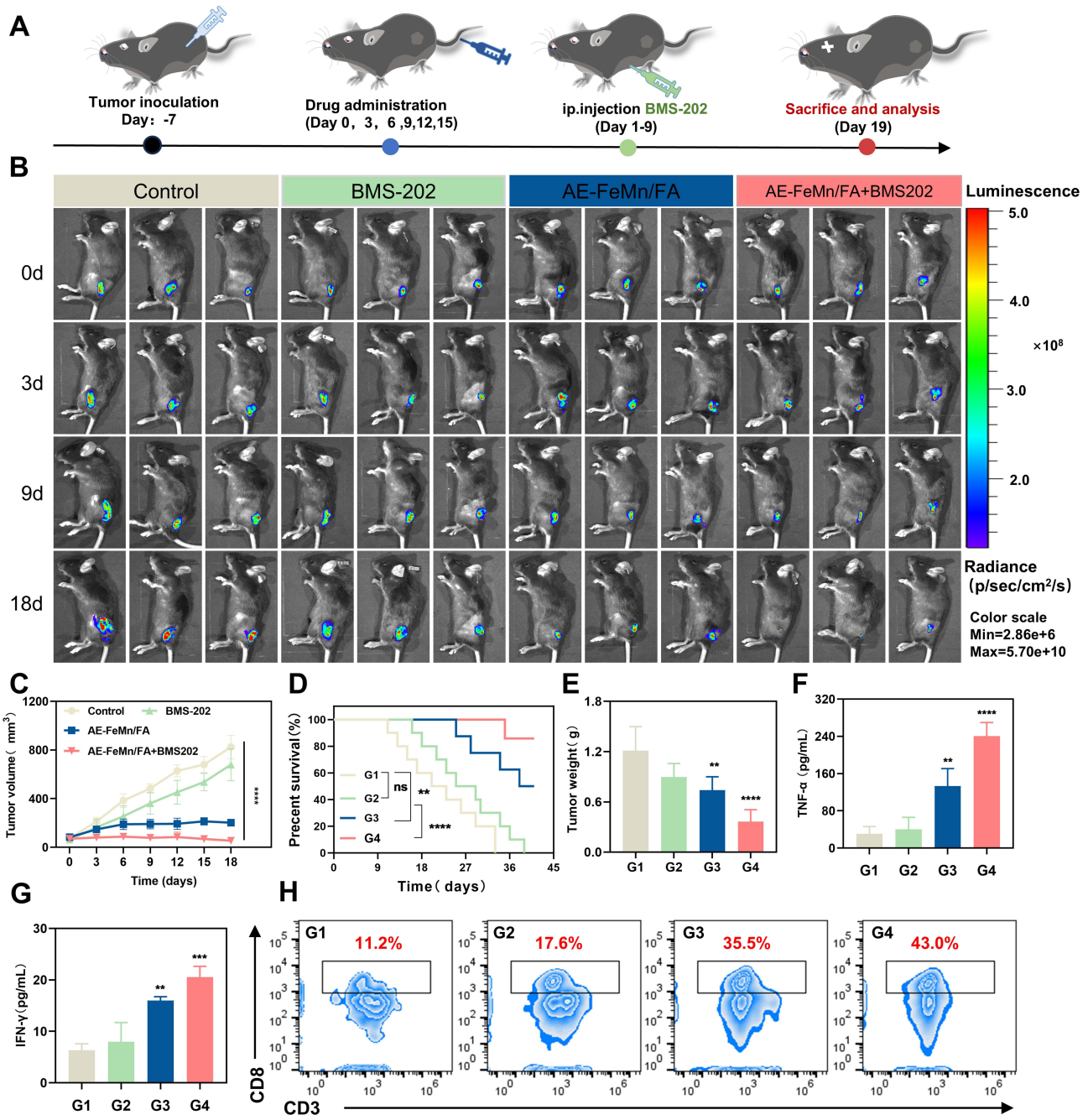

Figure 7 Evaluation of the antitumor effects of AE-FeMn/FA combined with BMS-202 immunotherapy. (**A**) Schematic illustration of the combined treatment with AE-FeMn /FA and BMS-202 to inhibit tumor growth. (**B**) In vivo bioluminescent imaging captured to track tumor growth on days 0, 3, 9, and 18. (**C**) Tumor growth curves in mice following various treatments (n = 6). (**D**) Survival curves of mice bearing Hepa1-6-Luc tumors (n = 10). Median survival (day): G1:21.5, G2:27, G3:39.5, G4: not reached (NR). (**E**) Tumor weights measured on day 19 (n = 6). Serum levels of immune-related cytokines following different treatments: (**F**) TNF-α and (**G**) IFN-γ (n=3). Representative flow cytometry results for CD8+ T cells (CD8+, CD3+) in tumor tissues after various treatments (**H**) along with corresponding quantitative analysis (**H**) (n=3, **P < 0.01, ***P < 0.001, ****P < 0.0001). (G1: Control; G2: BMS-202; G3:AE-FeMn/FA; G4: AE-FeMn/FA+ BMS202).

Additionally, the loaded AE further enhances the pyroptosis effect, causing the liberation of cytoplasmic contents associated with ICD. This process stimulates dendritic cell maturation, thereby inducing immunogenicity. Furthermore, the addition of BMS-202, a small molecule immune checkpoint inhibitor, further boosts the anti - neoplastic immune response stimulated by AE-FeMn/FA by inhibiting the PD-1/PD-L1 interactions. This combined strategy, which combines pyroptosis with the use of a small molecule immune checkpoint inhibitor, activates the innate immune response and transforms the immunosuppressed tumor microenvironment into an immunogenic one. These discoveries

offer a novel strategy for immunotherapy in HCC and hold significant potential for clinical translation. This work has important clinical implications and provides novel concepts and orientations for future research. Although this study confirms the therapeutic potential of AE-FeMn/FA in hepatocellular carcinoma, the safety of its clinical translation requires careful evaluation. It is noteworthy that the neurotoxicity of high-concentration Mn^{2+} has been reported in several previous studies,[55,56] which reminds us of the need to strictly define the scope of its safe application. Although the current data of this study show that Mn^{2+} causes no obvious damage to other major organs, there are still certain limitations: first, no more specific safety assessment has been conducted for the central nervous system; second, the lack of a long-term exposure model may fail to rule out the risk of chronic cumulative nerve damage. However, the concentration of Mn^{2+} used in this study has relatively high safety under the current experimental conditions. Fan et al[57] successfully remodeled the hypoxic and immunosuppressive tumor microenvironment using light-triggered nanozymes, which provides valuable insights for our research: we propose to introduce a light-triggered mechanism into the MOF-mediated delivery system in future studies to achieve precise and controllable drug release. This design not only enhances therapeutic efficacy but also helps mitigate the potential neurotoxic effects of Mn^{2+}. Nevertheless, we fully recognize the necessity of conducting systematic evaluations on the central nervous system. Therefore, future research will further focus on its long-term safety to provide more comprehensive evidence for the clinical application of Mn^{2+}.

In addition, compared with macromolecular ICBs antibodies such as pembrolizumab, BMS-202 has the advantages of small molecular weight and strong tissue penetrability, making it more easily enriched in the deep part of solid tumors via nanocarriers. However, it has a short half-life and is prone to causing off-target effects. Therefore, in this study, the AE-FeMn/FA nano-platform was used for delivery to prolong the action time through sustained release and reduce the impact on normal tissues through targeting. For future translational research, we plan to advance along the pathway from specific validation at the cellular level to long-term toxicity evaluation in animal models, and then to preclinical pharmacokinetic optimization. Nevertheless, practical challenges such as the biocompatibility standards of nanocarriers and the batch stability between small molecules and carriers need to be addressed, which will be the key breakthrough directions in subsequent studies. Luo et al[58] constructed a biomimetic targeted co-delivery system with excellent targeting ability and biocompatibility. This biomimetic design strategy can be adapted for the MOF-mediated aloe-emodin delivery system. For example, MOF materials could be coated with membrane components derived from tumor cells or related cells; alternatively, MOFs could be modified to specifically recognize surface markers of hepatocellular carcinoma cells. Such modifications would enable more precise targeted delivery, enhance the accumulation of aloe-emodin at tumor sites, and thereby improve therapeutic efficacy.

Meanwhile, the conclusion that "combined immunosuppressive therapy alleviates immunosuppression" in this study is primarily supported by indirect evidence. A major limitation of the current research lies in the failure to directly detect phenotypic changes in regulatory T cells (Tregs) and tumor-associated macrophages (TAMs), as well as the lack of direct measurement of PD-L1 expression levels in tumor tissues. To address these limitations, we plan to further validate the regulatory mechanism of the combined therapy on the PD-1/PD-L1 pathway and tumor immune microenvironment in future studies. Specifically, we will detect PD-L1 protein and mRNA expression levels in tumor tissues, perform PD-L1 neutralization experiments, and supplement phenotypic analyses of Tregs and TAMs to achieve a more comprehensive verification.

Funding

This study was supported by the following funding sources: the National Natural Science Foundation of China (Grant No. 82173010); the Beijing Huatong Guokang Public Welfare Foundation (Grant No. 2023HT028); and the Guangxi Science and Technology Bases and Talent Special Program, funded by the Guangxi Clinical Medical Research Center for Early Diagnosis and Treatment of Gastric Cancer (Grant No. 2022AC04006).

Disclosure

The researchers state that there are no recognized financial conflicts of interest or personal associations that might have seemingly affected the research presented in this article.

References

1. Chan TA, Yarchoan M, Jaffee E, et al. Development of tumor mutation burden as an immunotherapy biomarker: utility for the oncology clinic. *Ann Oncol*. 2019;30(1):44–56. doi:10.1093/annonc/mdy495
2. Budimir N, Thomas GD, Dolina JS, Salek-Ardakani S. Reversing T-cell exhaustion in cancer: lessons learned from PD-1/PD-L1 immune checkpoint blockade. *Cancer Immunol Res*. 2022;10(2):146–153. doi:10.1158/2326-6066.CIR-21-0515
3. Heinhuis KM, Ros W, Kok M, Steeghs N, Beijnen JH, Schellens JHM. Enhancing antitumor response by combining immune checkpoint inhibitors with chemotherapy in solid tumors. *Ann Oncol*. 2019;30(2):219–235. doi:10.1093/annonc/mdy551
4. Dolina JS, Lee J, Brightman SE, et al. Linked CD4+/CD8+ T cell neoantigen vaccination overcomes immune checkpoint blockade resistance and enables tumor regression. *J Clin Invest*. 2023;133(17):e164258. doi:10.1172/JCI164258
5. Lin M, He J, Zhang X, et al. Targeting fibrinogen-like protein 1 enhances immunotherapy in hepatocellular carcinoma. *J Clin Invest*. 2023;133(9):e164528. doi:10.1172/JCI164528
6. Wang SJ, Dougan SK, Dougan M. Immune mechanisms of toxicity from checkpoint inhibitors. *Trends Cancer*. 2023;9(7):543–553. doi:10.1016/j.trecan.2023.04.002
7. Chen L, Zhao X, Liu X, Ouyang Y, Xu C, Shi Y. Development of small molecule drugs targeting immune checkpoints. *Cancer Biol Med*. 2024;21(5):382–399. doi:10.20892/j.issn.2095-3941.2024.0034
8. Gu Y, Zhang Z, Ten Dijke P. Harnessing epithelial-mesenchymal plasticity to boost cancer immunotherapy. *Cell Mol Immunol*. 2023;20(4):318–340. doi:10.1038/s41423-023-00980-8
9. Petitprez F, Meylan M, de Reyniès A, Sautès-Fridman C, Fridman WH. The tumor microenvironment in the response to immune checkpoint blockade therapies. *Front Immunol*. 2020;11:784. doi:10.3389/fimmu.2020.00784
10. Bejarano L, Jordão MJC, Joyce JA. Therapeutic targeting of the tumor microenvironment. *Cancer Discov*. 2021;11(4):933–959. doi:10.1158/2159-8290.CD-20-1808
11. Polak R, Zhang ET, Kuo CJ. Cancer organoids 2.0: modelling the complexity of the tumour immune microenvironment. *Nat Rev Cancer*. 2024;24(8):523–539. doi:10.1038/s41568-024-00706-6
12. Rao Z, Zhu Y, Yang P, et al. Pyroptosis in inflammatory diseases and cancer. *Theranostics*. 2022;12(9):4310–4329. doi:10.7150/thno.71086
13. Hsu SK, Li CY, Lin IL, et al. Inflammation-related pyroptosis, a novel programmed cell death pathway, and its crosstalk with immune therapy in cancer treatment. *Theranostics*. 2021;11(18):8813–8835. doi:10.7150/thno.62521
14. Ding B, Chen H, Tan J, et al. ZIF-8 nanoparticles evoke pyroptosis for high-efficiency cancer immunotherapy. *Angew Chem Int Ed Engl*. 2023;62(10):e202215307. doi:10.1002/anie.202215307
15. Dai Y, Guo Z, Leng D, et al. Metal-coordinated NIR-II nanoadjuvants with nanobody conjugation for potentiating immunotherapy by tumor metabolism reprogramming. *Adv Sci*. 2024;11(34):e2404886. doi:10.1002/advs.202404886
16. Chi H, Zhu G, Yin Y, et al. Dual-responsive multifunctional "core-shell" magnetic nanoparticles promoting Fenton reaction for tumor ferroptosis therapy. *Int J Pharm*. 2022;622:121898. doi:10.1016/j.ijpharm.2022.121898
17. Feng Z, Chen G, Zhong M, et al. An acid-responsive MOF nanomedicine for augmented anti-tumor immunotherapy via a metal ion interference-mediated pyroptotic pathway. *Biomaterials*. 2023;302:122333. doi:10.1016/j.biomaterials.2023.122333
18. Li J, Ma S, Lin Q, et al. Orchestrated copper-loaded nanoreactor for simultaneous induction of cuproptosis and immunotherapeutic intervention in colorectal cancer. *Mater Today Bio*. 2024;29:101326. doi:10.1016/j.mtbio.2024.101326
19. Wang D, Zhang M, Zhang Y, et al. Intraparticle double-scattering-decoded sonogenetics for augmenting immune checkpoint blockade and CAR-T therapy. *Adv Sci*. 2022;9(32):e2203106. doi:10.1002/advs.202203106
20. Wang D, Nie T, Huang C, et al. Metal-cyclic dinucleotide nanomodulator-stimulated STING signaling for strengthened radioimmunotherapy of large tumor. *Small*. 2022;18(41):e2203227. doi:10.1002/smll.202203227
21. Xia C, Xing X, Zhang W, et al. Cysteine and homocysteine can be exploited by GPX4 in ferroptosis inhibition independent of GSH synthesis. *Redox Biol*. 2024;69:102999. doi:10.1016/j.redox.2023.102999
22. Liu G, Liu M, Li X, et al. Peroxide-simulating and GSH-depleting nanozyme for enhanced chemodynamic/photodynamic therapy via induction of multisource ROS. *ACS Appl Mater Interfaces*. 2023;15(41):47955–47968. doi:10.1021/acsami.3c09873
23. Du Q, Luo Y, Xu L, et al. Smart responsive Fe/Mn nanovaccine triggers liver cancer immunotherapy via pyroptosis and pyroptosis-boosted cGAS-STING activation. *J Nanobiotechnology*. 2024;22(1):95. doi:10.1186/s12951-024-02354-2
24. Wang D, Qiu G, Zhu X, et al. Macrophage-inherited exosome excise tumor immunosuppression to expedite immune-activated ferroptosis. *J Immunother Cancer*. 2023;11(5):e006516. doi:10.1136/jitc-2022-006516
25. Yang J, Yang YW. Metal-organic frameworks for biomedical applications. *Small*. 2020;16(10):e1906846. doi:10.1002/smll.201906846
26. Dong X, Zeng Y, Liu Y, et al. Aloe-emodin: a review of its pharmacology, toxicity, and pharmacokinetics. *Phytother Res*. 2020;34(2):270–281. doi:10.1002/ptr.6532
27. Yu J, Zhao X, Yan X, et al. Aloe-emodin ameliorated MI-induced cardiac remodeling in mice via inhibiting TGF-β/SMAD signaling via up-regulating SMAD7. *Phytomedicine*. 2023;114:154793. doi:10.1016/j.phymed.2023.154793
28. Zhu M, He Q, Wang Y, et al. Exploring the mechanism of aloe-emodin in the treatment of liver cancer through network pharmacology and cell experiments. *Front Pharmacol*. 2023;14:1238841. doi:10.3389/fphar.2023.1238841
29. He Y, Xi J, Fang J, Zhang B, Cai W. Aloe-emodin alleviates doxorubicin-induced cardiotoxicity via inhibition of ferroptosis. *Free Radic Biol Med*. 2023;206:13–21. doi:10.1016/j.freeradbiomed.2023.06.025
30. Li X, Yao M, Li L, et al. Aloe-emodin alleviates cerebral ischemia-reperfusion injury by regulating microglial polarization and pyroptosis through inhibition of NLRP3 inflammasome activation. *Phytomedicine*. 2024;129:155578. doi:10.1016/j.phymed.2024.155578
31. Yu Z, Cao L, Shen Y, et al. Inducing cuproptosis with copper ion-loaded aloe emodin self-assembled nanoparticles for enhanced tumor photodynamic immunotherapy. *Adv Healthc Mater*. 2025;14(9):e2404612. doi:10.1002/adhm.202404612
32. Wu M, Ling W, Wei J, et al. Biomimetic photosensitizer nanocrystals trigger enhanced ferroptosis for improving cancer treatment. *J Control Release*. 2022;352:1116–1133. doi:10.1016/j.jconrel.2022.11.026
33. Şeker Karatoprak G, Küpeli Akkol E, Yücel Ç, Bahadır Acıkara Ö, Sobarzo-Sánchez E. Advances in understanding the role of aloe emodin and targeted drug delivery systems in cancer. *Oxid Med Cell Longev*. 2022;2022:7928200. doi:10.1155/2022/7928200

34. Chen R, Zhang J, Hu Y, Wang S, Chen M, Wang Y. Potential antineoplastic effects of Aloe-emodin: a comprehensive review. *Am J Chin Med*. 2014;42(2):275–288. doi:10.1142/S0192415X14500189
35. Chen Y, Liu W, Shang Y, et al. Folic acid-nanoscale gadolinium-porphyrin metal-organic frameworks: fluorescence and magnetic resonance dual-modality imaging and photodynamic therapy in hepatocellular carcinoma. *IJN*. 2018;Volume 14:57–74. doi:10.2147/IJN.S177880
36. Hu Z, Chen J, Zhou S, et al. Mouse IP-10 gene delivered by folate-modified chitosan nanoparticles and dendritic/tumor cells fusion vaccine effectively inhibit the growth of hepatocellular carcinoma in mice. *Theranostics*. 2017;7(7):1942–1952. doi:10.7150/thno.16236
37. Liu M, Tu J, Feng Y, Zhang J, Wu J. Synergistic co-delivery of diacid metabolite of norcantharidin and ABT-737 based on folate-modified lipid bilayer-coated mesoporous silica nanoparticle against hepatic carcinoma. *J Nanobiotechnol*. 2020;18(1):114. doi:10.1186/s12951-020-00677-4
38. Liu S, Pan J, Liu J, et al. Dynamically PEGylated and borate-coordination-polymer-coated polydopamine nanoparticles for synergetic tumor-targeted, chemo-photothermal combination therapy. *Small*. 2018;14(13):e1703968. doi:10.1002/smll.201703968
39. Lin LS, Song J, Song L, et al. Simultaneous fenton-like ion delivery and glutathione depletion by mno2 -based nanoagent to enhance chemodynamic therapy. *Angew Chem Int Ed Engl*. 2018;57(18):4902–4906. doi:10.1002/anie.201712027
40. Chen W, Hu F, Gao Q, et al. Tumor acidification and GSH depletion by bimetallic composite nanoparticles for enhanced chemodynamic therapy of TNBC. *J Nanobiotechnology*. 2024;22(1):98. doi:10.1186/s12951-024-02308-8
41. Jia T, Wang Z, Sun Q, et al. Intelligent Fe-Mn layered double hydroxides nanosheets anchored with upconversion nanoparticles for oxygen-elevated synergetic therapy and bioimaging. *Small*. 2020;16(46):e2001343. doi:10.1002/smll.202001343
42. Zhang L, Li CX, Wan SS, Zhang XZ. Nanocatalyst-mediated chemodynamic tumor therapy. *Adv Healthc Mater*. 2022;11(2):e2101971. doi:10.1002/adhm.202101971
43. Loveless R, Bloomquist R, Teng Y. Pyroptosis at the forefront of anticancer immunity. *J Exp Clin Cancer Res*. 2021;40(1):264. doi:10.1186/s13046-021-02065-8
44. Kovacs SB, Miao EA. Gasdermins: effectors of Pyroptosis. *Trends Cell Biol*. 2017;27(9):673–684. doi:10.1016/j.tcb.2017.05.005
45. Fang X, Chen Z, Zhou W, et al. Boosting glioblastoma therapy with targeted pyroptosis induction. *Small*. 2023;19(30):2207604. doi:10.1002/smll.202207604
46. Tan Y, Chen Q, Li X, et al. Pyroptosis: a new paradigm of cell death for fighting against cancer. *J Exp Clin Cancer Res*. 2021;40(1):153. doi:10.1186/s13046-021-01959-x
47. Yang F, Bettadapura SN, Smeltzer MS, Zhu H, Wang S. Pyroptosis and pyroptosis-inducing cancer drugs. *Acta Pharmacol Sin*. 2022;43(10):2462–2473. doi:10.1038/s41401-022-00887-6
48. Mannion J, Gifford V, Bellenie B, et al. A RIPK1-specific PROTAC degrader achieves potent antitumor activity by enhancing immunogenic cell death. *Immunity*. 2024;57(7):1514–1532.e15. doi:10.1016/j.immuni.2024.04.025
49. Huang Z, Wang Y, Yao D, Wu J, Hu Y, Yuan A. Nanoscale coordination polymers induce immunogenic cell death by amplifying radiation therapy mediated oxidative stress. *Nat Commun*. 2021;12(1):145. doi:10.1038/s41467-020-20243-8
50. Huang C, Lin B, Chen C, et al. Synergistic reinforcing of immunogenic cell death and transforming tumor-associated macrophages via a multifunctional cascade bioreactor for optimizing cancer immunotherapy. *Adv Mater*. 2022;34(51):e2207593. doi:10.1002/adma.202207593
51. Sugiura D, Okazaki IM, Maeda TK, et al. PD-1 agonism by anti-CD80 inhibits T cell activation and alleviates autoimmunity. *Nat Immunol*. 2022;23(3):399–410. doi:10.1038/s41590-021-01125-7
52. Zhu Y, Chen M, Xu D, et al. The combination of PD-1 blockade with interferon-α has a synergistic effect on hepatocellular carcinoma. *Cell Mol Immunol*. 2022;19(6):726–737. doi:10.1038/s41423-022-00848-3
53. Yang X, Wang W, Ji T. Metabolic remodeling by the PD-L1 inhibitor BMS-202 significantly inhibits cell malignancy in human glioblastoma. *Cell Death Dis*. 2024;15(3):186. doi:10.1038/s41419-024-06553-5
54. Kheraldine H, Gupta I, Cyprian FS, et al. Targeting HER2-positive breast cancer cells by a combination of dasatinib and BMS-202: insight into the molecular pathways. *Cancer Cell Int*. 2024;24(1):94. doi:10.1186/s12935-023-03195-z
55. Pajarillo E, Nyarko-Danquah I, Digman A, et al. Mechanisms of manganese-induced neurotoxicity and the pursuit of neurotherapeutic strategies. *Front Pharmacol*. 2022;13:1011947. doi:10.3389/fphar.2022.1011947
56. Khindri NM, Maj MC. Manganese-induced parkinsonism: a review of etiologies and treatments. *Degener Neurol Neuromuscul Dis*. 2025;15:65–79. doi:10.2147/DNND.S482018
57. Fan Z, Wu S, Deng H, Li G, Huang L, Liu H. Light-triggered nanozymes remodel the tumor hypoxic and immunosuppressive microenvironment for ferroptosis-enhanced antitumor immunity. *ACS Nano*. 2024;18(19):12261–12275. doi:10.1021/acsnano.4c00844
58. Luo T, Fan Z, Zeng A, et al. Biomimetic targeted co-delivery system engineered from genomic insights for precision treatment of osteosarcoma. *Adv Sci*. 2025;12(2):e2410427. doi:10.1002/advs.202410427